USING MACRO-FIBER COMPOSITE ACTUATORS FOR AQUATIC LOCOMOTION

BY

ZACHARY PATRICK HILLS

Thesis submitted to the faculty of the Virginia Polytechnic Institute and State University in partial fulfillment of the requirements for the degree of

MASTER OF SCIENCE

IN

MECHANICAL ENGINEERING

Daniel J. Inman, Chair

Shashank Priya

Shane D. Ross

May 20, 2010

Blacksburg, Virginia

Keywords: Piezoelectric, MFC, Carangiform, Locomotion

Copyright by Zachary Patrick Hills, 2010

USING MACRO-FIBER COMPOSITE ACTUATORS FOR AQUATIC LOCOMOTION

ZACHARY PATRICK HILLS

ABSTRACT

The research presented herein aims to develop a bio-inspired swimming system for an autonomous underwater vehicle using Macro-Fiber Composite (MFC) actuators. The swimming system draws inspiration from the motion of carangiform fish, which limit their body motion while rapidly oscillating their caudal tail fin. The foundation for the bio-inspired swimming system is built upon a composite cantilever beam with MFC actuators in bimorph configuration. The MFC actuators excite the composite beam near its fundamental natural frequency to produce thrust as the vibration transfers momentum to the surrounding fluid. An analytical model that incorporates Euler-Bernoulli beam theory, linear piezoelectricity, and fluid mechanics is developed to predict the thrust generated by the beam vibration. Experimental testing is performed to verify aspects of, as well as recommend corrections to, the analytical model. A prototype carangiform swimmer is developed that employs a passive caudal tail fin to alter the vibratory motion of the system from a beam vibration mode to one more resembling carangiform swimming. This device is subjected to experimental testing to determine the swim speeds it is able to achieve. A maximum velocity of 90mm/s was observed when the system is excited at 900V. However, better performance may be achieved by increasing the excitation voltage.

DEDICATION

To my wife, Holly, and my parents, Richard and Christine, for their unconditional love, support, and inspiration.

ACKNOWLEDGEMENTS

My sincerest gratitude is presented to Dr. Daniel J. Inman, my advisor, for his tutelage and support during this arduous time known as graduate school. Special thanks are offered to Dr. Myung Hyun Kim, whom provided me with an abundance of guidance and assistance throughout this research. I would also like to thank Dr. Shashank Priya for orchestrating the MURI project that oversaw this research as well as for serving on my committee. Additional thanks are offered to Dr. Shane D. Ross for also serving on my committee and for continuing to fuel my passion of dynamical systems.

My colleagues at the Center for Intelligent Material Systems and Structures (CIMSS) have provided me with limitless support and guidance that has significantly impacted this research. Without their assistance, I would be eternally trapped in the laboratory attempting to resolve various experimentation and modeling issues that plagued this research.

Lastly, I would like to gratefully acknowledge the financial support from Office of Naval Research through MURI Grant # N00014-08-1-0654 that funded this research.

TABLE OF CONTENTS

LIST OF FIGURES

LIST OF TABLES

1 INTRODUCTION

1.1 MOTIVATION

Evolution has produced countless, highly specialized life forms that have adapted to survive in a variety of environments. One recent research trend is to develop engineering systems that are inspired by these highly specialized, as well as highly energy efficient, life forms. The motivation behind this study is to develop a bio-inspired swimming system for an autonomous underwater vehicle using Macro-Fiber Composite (MFC) actuators. MFC actuators are recently developed smart material solid-state actuators based on the piezoelectric effect. The swimming system employs a composite cantilever beam that has MFC actuators in bimorph configuration. The MFC actuators drive the composite beam at its fundamental natural frequency, which produces thrust as momentum is imparted to the surrounding fluid due to the beam vibration. This cantilever beam swimming system draws inspiration from the tail motion of carangiform fish, which are simple and efficient swimmers that produce forward momentum by rapidly oscillating their tail at large amplitude while limiting their body motion.

1.2 LITERATURE REVIEW

1.2.1 SWIMMING SYSTEM MODELS

The first known attempt to describe the tail motion of a swimming organism from a hydrodynamic point of view was by Taylor [1]. Taylor modeled the tail of a spermatozoon as a flexible cylinder that is distorted by waves of lateral displacement propagating along its length. Taylor elected to model the spermatozoon tail as a flexible cylinder because variations in cross-sectional area have a minimal influence on the system dynamics when the Reynolds number is small. Forward momentum results from waves in the fluid that propagate backwards along the spermatozoon tail as a result of the tail motion. Attempts by Taylor to experimentally validate this model were largely unsuccessful.

Lighthill [2] developed a model that incorporated vortex shedding when determining the swimming motion necessary for a slender fish to have a high Froude propulsive efficiency. The Froude propulsive efficiency is the ratio of the forward velocity multiplied by thrust available to overcome frictional drag to the work done to produce both thrust and vortex wake. The components of the Froude propulsive efficiency are determined using slender body theory in conjunction with inviscid-flow theory. Lighthill [3] expanded upon his previous model by employing elongated-body theory to account for large amplitude motion. This expanded model predicted the instantaneous reactive force between the fish and water for arbitrary fish motion. Lighthill compared analytical simulation results with experimental data on the carangiform swimmer Leuciscus.

Lighthill's work on the fluid dynamics of swimming fish has contributed heavily to the modeling, as well as the development of, bio-inspired swimming systems. Subsequent research by Sfakiotakis et al [4] produced a relatively comprehensive overview discussing the various fish swimming modes used in aquatic locomotion that relied, in part, on work done by Lighthill. More recently, Mollendorf et al [5] expanded upon Lighthill's work by developing an analytical solution for steady-periodic vibration of a thin elastic beam subject to hydrodynamic loading with applications towards dive fins. Yu et al [6] presented a simplified propulsive model for carangiform swimming based on Lighthill's work. The model was unable to be successfully verified using a bio-mimetic carangiform fish due to oversimplifications in the device's control system.

1.2.2 Bio-Inspired Swimming Systems Using Smart Materials

The recent push towards bio-inspired engineering has resulted in the development of fishlike micro-robots that use several different actuation technologies, which includes multiple classes of smart materials. Smart materials are materials that exhibit coupling between two domains. For example, the mechanical and electrical domains are coupled in piezoelectric materials. A voltage is produced when the material is strained and, conversely, strain is produced when a voltage is applied. The types of smart materials that have been used in the

development of fishlike micro-robots include ionic conducting polymer film actuators, magnetostrictive actuators, shape memory alloy actuators, and piezoelectric actuators.

1.2.2.1 IONIC CONDUCTING POLYMER SWIMMING SYSTEMS

Ionic conducting polymer film (ICPF) actuators are smart material actuators that utilize electromechanical coupling from charge transport to produce mechanical motion. A significant amount of work has been done in both China and Japan using ICPF actuators to develop a micro-robot carangiform swimmer. Guo et al [7] developed a micro-robot carangiform swimmer with two tails containing ICPF actuators made from Du Pont's Nafion 117. Each tail section was controlled individually to provide rudimentary steering control. Additionally, preliminary experimental results indicated the micro-robot's maximum velocity was a function of the input voltage's amplitude and frequency. Guo et al subsequently developed a series of increasingly complex prototypes while expanding upon these results in [8, 9]. Guo also oversaw the work of Ye et al [10], which produced a micro-robot swimmer driven by a single Nafion 117 ICPF actuated tail section. Ye et al [11] later developed a micro-robot swimmer that incorporated pectoral fins as well as a caudal tail fin. Adding pectoral fins to the micro-robot increased both linear and turning velocities when compared to micro-robots only using a caudal tail fin. This device was able to maintain linear speeds of approximately 35mm/s when driven at 1.2Hz.

1.2.2.2 MAGNETOSTRICTIVE SWIMMING SYSTEMS

Magnetostrictive materials are smart materials that couple mechanical motion with the applied magnetic field. There have been several micro-robots designed and fabricated using magnetostrictive materials. Honda et al [12] developed a micro-robot that used a small magnet attached to a spiral wire to produce thrust. Applying an external, alternating magnetic field to the micro-robot produced a magnetic torque that would rotate the small magnet. The rotation produced waves that travelled along the spiral, propelling the micro-robot forward. Sudo et al [13] discussed a similar propulsion system for medical micro-robots designed to work in human blood vessels that used an alternating magnetic field to wirelessly drive neodymium magnets. Propulsion characteristics as well as the effects of fluid viscosity were studied experimentally for the medical micro-robot. Pan and Guo [14] developed several bio-mimetic, magnetically

controlled micro-robots designed to work in confined spaces, such as blood vessels. Directional control was achieved by varying the frequency of the input current that governs the magnetic field. Guo et al [15] expanded upon this work to include additional prototype configurations. Zhang and Liu [16] developed a bidirectional wireless swimming micro-robot that employed fin beating propulsion. Fins made from giant magnetostrictive films are placed at opposite ends of the micro-robot to achieve bidirectional motion. The design's feasibility was demonstrated through theoretical analysis and experimental testing.

1.2.2.3 Shape Memory Alloy Swimming Systems

Shape memory alloys (SMA) are thermomechanically coupled smart materials that produce large mechanical strains when heated and cooled. Additionally, metallic shape memory alloys can produce large mechanical stresses when thermally loaded. SMAs have received more attention than any other smart material due to their large deformation for designing bio-inspired swimming systems. Accordingly, several different actuation design methodologies have been proposed and implemented in the literature. Rediniotis et al [17] developed a 2-D flapping hydrofoil with embedded SMAs that oscillate the hydrofoil's trailing edge to generate thrust. Experimental data was compared with a finite element model that predicts hydrofoil behavior. Subsequent work has been done over the years on this project to improve the hydrofoil design and finite element analysis [18-21]. Zhang et al [22-26] published a series of papers on a SMA swimming system that was capable of both oscillatory and undulatory motion inspired by rays. Analytical as well as numerical models were developed to support this work. Ono et al [27] proposed a SMA based swimming system for a hammerhead shark inspired robot. Cho et al [28] designed and fabricated a centimeter-scale subcarangiform swimming system that utilized several SMA springs to articulate a jointed fish micro-robot. Another subcarangiform swimming system created by Wang et al [29] achieved similar results by controlling a bio-mimetic SMA fin that drives a passive caudal fin. This device swam at 112mm/s when driven at 2.5Hz.

1.2.2.4 Piezoelectric Swimming Systems

As previously mentioned, piezoelectric materials are electromechanically coupled smart materials that produce a voltage when strained and, conversely, produce strain when a voltage

is applied. Fukuda et al [30] created the first fishlike micro-robot to use piezoelectric transducers. The 1-D micro-robot used dual, symmetrically excited fins made from lead zirconate titanate (PZT) to generate thrust. Fukuda et al [31, 32] updated the micro-robot to include steering control to allow for 2-D motion. Borgen et al [33] developed a miniature swimming vehicle that propels itself by a vibrating flexible fin mounted in the stern. Two curved-beam bending piezoelectric actuators made from PZT drive the flexible fin. Heo et el [34] constructed a full-scale bio-mimetic fish that used two unimorph piezoelectric bending beams to control a rack-and-pinion system which, in turn, vibrated the caudal tail fin. Additional work has been conducted on this system by Wiguna et al [35, 36]. Another propulsion scheme for micro-robots has been developed by Kosa et al [37], which uses dual tails that are divided into three segments. The piezoelectric material in each section is excited at different frequencies to produce travelling waves that generate thrust.

1.2.3 The Macro-Fiber Composite

Macro-Fiber Composites are piezoceramic composite solid-state actuators that were recently developed at NASA's Langley Research Center [38]. While it is possible to manufacture MFCs using the techniques provided by High and Wilke [39], most end-users elect to purchase the devices from the NASA licensed supplier Smart Material Corporation. MFCs are made from piezocomposite sheets that have been sandwiched between layers of structural epoxy and a polyimide film that has embedded interdigitated copper electrodes. The piezocomposite sheets consist of aligned rectangular piezoceramic fibers made from PZT-5A that are placed inside a matrix polymer for strength and protection. Additionally, this structure allows the MFC to be far more flexible and conformable than a monolithic piezoceramic. A schematic highlighting the structure of a MFC is shown in Figure 1.1.

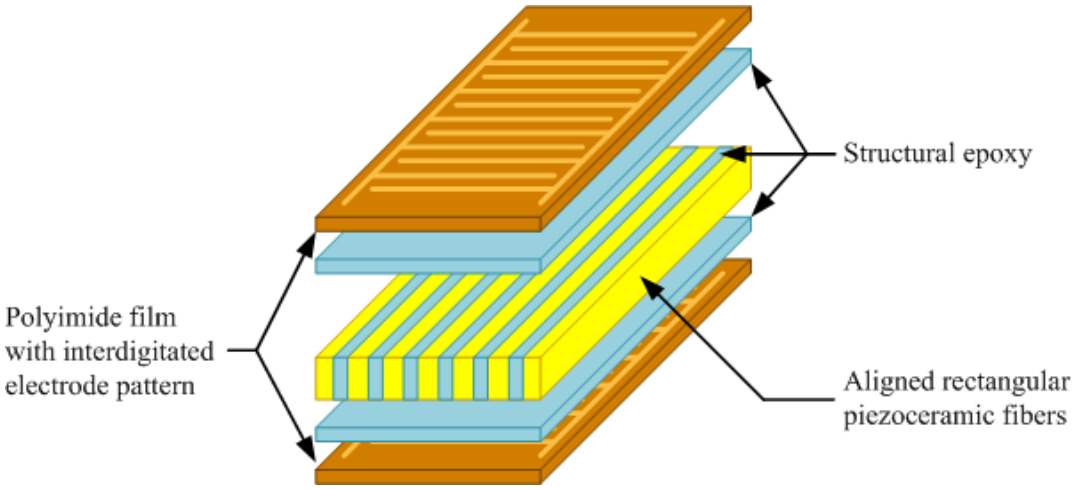

FIGURE 1.1 STRUCTURAL SCHEMATIC FOR A TYPICAL MACRO-FIBER COMPOSITE ACTUATOR.

The interdigitated electrode pattern allows the piezoceramic to be poled and actuated in-plane using the d_{33} effect, whereas a typical monolithic piezoceramic uses the d_{31} effect. This is advantageous because the d_{33} effect is approximately 2.4 times larger than the d_{31} effect for typical piezoceramics. Therefore, significantly larger strains are produced when using the 33-mode than when using the 31-mode. As such, the in-plane poling on the MFC will provide better performance, i.e. larger tip displacements, when driving a bending beam than a monolithic piezoceramic.

1.2.3.1 MACRO-FIBER COMPOSITE APPLICATIONS

Macro-Fiber Composites, much like other piezoelectric materials, are frequently used for actuation and energy harvesting applications. Since there is a wealth of literature that discusses the various additional MFC applications, this review shall only discuss work directly related to hydrodynamic propulsion. Bilgen et al [40, 41] developed a series of variable camber airfoils that used MFC actuators to change airfoil camber during flight. Subsequent work by Bilgen et al [42] led to the development of unimorph benders which are direct predecessors to the MFC swimming system discussed herein. Additionally, energy harvesting research conducted by Erturk et al [43] has lead to the derivation of an experimental model that characterizes the piezoelectric forcing function for a MFC.

1.2.3.2 MACRO-FIBER COMPOSITE SWIMMING SYSTEMS

Little work to date has been undertaken that focuses on using MFCs to develop a bio-inspired swimming system. Wang et al [44] created a fishlike robot with two forked tails that employed MFC actuators in the propulsions system. The propulsion system was made from a curved aluminum bending beam that was supported at its midpoint and had a unimorph MFC bonded to its centerline. The curved beam vibrates symmetrically about its midpoint when voltage was applied to the MFC. Passive fins were attached to the free ends of the curved beam, which creates two forked tails that produce thrust when driven by the MFC. The robot was experimentally tested using various fin geometries in an attempt to maximize thrust.

Two additional bio-inspired swimming robots that use MFCs actuators for propulsion have been developed Nagata et al [45]. The first robot presented used a single MFC actuator that is bonded lengthwise onto an irregularly shaped carbon plate. The carbon plate's geometry was such that a triangular region of the carbon plate extends beneath the MFC actuator in an attempt to increase the thrust output. Experimental results showed correlations between propulsive force and excitation frequency as well as between excitation voltage and swimming velocity. The second robot presented used two MFC actuators placed sequentially and on opposite sides of a carbon beam. Controlling each actuator individually enabled the device to have bi-directional swimming and the ability to station keep. Subsequent work by Ming et al [46] included a brief analytical analysis of the propulsive force generated by a meandering swimmer. This work also presents a free-swimming robotic fish that used a beam with bimorph MFC actuators to drive a passive tail. Experimental data presented the relationship between turning velocity and actuation frequency.

1.3 THESIS OVERVIEW

1.3.1 RESEARCH OBJECTIVES

The objective of this research has been to develop a bio-inspired swimming system for an autonomous underwater vehicle that generates thrust from the flapping motion produced by a cantilever beam driven at resonance by Macro-Fiber Composite actuators. To accomplish this

task, several different beam geometries, along with various actuator configurations, are considered as well as tested experimentally. Euler-Bernoulli beam theory is coupled with linear piezoelectricity and fluid mechanics to produce an analytical model that relates the voltage applied to the MFC actuators to the output thrust and maximum velocity. Experimental testing is employed in an attempt to verify the analytical model. A prototype swimmer is developed that transforms the flapping motion of a cantilever beam into a carangiform, or fishlike, swimming motion.

1.3.2 THESIS OUTLINE

A model for the vibration of a cantilever beam with MFC actuators in bimorph configuration that is immersed in a fluid as well as a model for the thrust produced by such a beam is derived in Chapter 2. The model varies from that of a typical beam vibrating in air because it includes an added mass term that accounts for the mass loading of the water and a drag term that accounts for the drag forces that result as the beam vibrates in the fluid. This chapter also provides a review of Euler-Bernoulli beam theory and linear piezoelectricity. Chapter 3 presents a series of experiments that attempt to verify the models developed in Chapter 2. The initial round of experimentation validates the added mass assumption included in the models. Subsequent experiments measure the thrust produced by composite cantilever beams that vibrate in water in an attempt to validate the hydrodynamic thrust model developed in Chapter 2. Validation of the hydrodynamic thrust model is met with mixed results. A novel prototype carangiform swimmer is developed in Chapter 4. The carangiform swimmer uses a fishlike substrate that includes a passive caudal tail fin to transform the flapping motion of a cantilever beam excited as its first mode into a carangiform-like motion. Conclusions regarding this work are drawn in Chapter 5.

2 THEORY

2.1 OVERVIEW OF TRANSVERSE BEAM VIBRATION

Simple mass-spring models are derived under lumped parameter assumptions, which assume the mass and stiffness are concentrated at specific points. Naturally, the lumped parameter assumptions do not apply to continuous systems, such as beams, because the mass and stiffness are distributed throughout the structure. Therefore, a distributed parameter model that accounts for the mass and stiffness distribution must be employed to accurately model the transverse vibration of a beam. The classical distributed parameter model for the transverse vibration of a beam is Euler-Bernoulli beam theory [47]. Euler-Bernoulli beam theory only applies to long, slender beams that have length to thickness ratios much greater than one as well as length to width ratios on the order of ten to one or greater.

For a simple clamped-free cantilever beam undergoing free vibration, Euler-Bernoulli beam theory states the equation of motion for the system as

$$\mu(x)\frac{\partial^2 w(x,t)}{\partial t^2}+\frac{\partial^2}{\partial x^2}\left[EI(x)\frac{\partial^2 w(x,t)}{\partial x^2}\right]=F(x,t) \tag{2.1.1}$$

where $w(x,t)$ is the transverse displacement of the beam as a function of both space and time, $\mu(x)$ is the mass density per unit length, $EI(x)$ is the bending stiffness, and $F(x,t)$ is arbitrary force applied to the beam. Four boundary conditions and two initial conditions are needed to solve Equation (2.1.1) since the equation contains four spatial partial derivatives and two temporal partial derivatives. The boundary conditions for the clamped boundary of a cantilever beam, which is assumed to be at the origin, are given as

$$w(x,t)\big|_{x=0}=w_x(x,t)\big|_{x=0}=0 \tag{2.1.2}$$

where the subscript x denotes a single partial derivative with respect to x. The first term prohibits motion at the fixed boundary while the second term prohibits slope. Similarly, the boundary conditions at the free boundary of the cantilever beam are given as

$$EI(x)\frac{\partial^2 w(x,t)}{\partial x^2}\bigg|_{x=L} = \frac{\partial}{\partial x}\left[EI(x)\frac{\partial^2 w(x,t)}{\partial x^2}\right]\bigg|_{x=L} = 0 \tag{2.1.3}$$

where the first term prohibits a bending moment from occurring at the free end while the second term prohibits shear. The initial conditions, for simplicity, are typically chosen such that both the initial displacement and velocity are zero:

$$w(x,t)\big|_{t=0} = \dot{w}(x,t)\big|_{t=0} = 0 \tag{2.1.4}$$

where the dot superscript corresponds to a single temporal derivative.

2.2 Overview of Linear Piezoelectricity

Modeling the electromechanical coupling exhibited by linear piezoelectric materials is a relatively well understood process [48]. Three dimensional linear piezoelectric systems are governed by the coupled constitutive equations:

$$\begin{aligned} \boldsymbol{S} &= \boldsymbol{s}^E \boldsymbol{T} + \boldsymbol{d}' \boldsymbol{E} \\ \boldsymbol{D} &= \boldsymbol{d}\boldsymbol{T} + \boldsymbol{\varepsilon}^T \boldsymbol{E} \end{aligned} \tag{2.2.1}$$

where $\boldsymbol{S}$ is a 6x1 vector of strains, $\mathbf{s}^E$ is a 6x6 matrix of compliance coefficients, $\boldsymbol{T}$ is a 6x1 vector of stresses, $\mathbf{d}$ is a 3x6 matrix of piezoelectric strain coefficients, $\boldsymbol{E}$ is a 3x1 vector of electric fields, $\boldsymbol{D}$ is a 3x1 vector of the electric displacements, and $\boldsymbol{\varepsilon}^T$ is a 3x3 matrix of dielectric permittivity values. For a one dimensional linear piezoelectric system, the coupled constitutive equations reduce to

$$\begin{Bmatrix} S \\ D \end{Bmatrix} = \begin{bmatrix} s & d \\ d & \varepsilon \end{bmatrix} \begin{Bmatrix} T \\ E \end{Bmatrix} \tag{2.2.2}$$

where each component in the constitutive relationships has reduced from a vector or matrix to a single term.

It should be noted that the standard convention for modeling piezoelectric devices is to align the polarization direction within the piezoelectric material to the 3-axis. Under this

convention, the two most common operating modes for piezoelectric devices utilize either the stress and strain produced along the axis of polarization, called the 33-mode, or those produced perpendicular to the axis of polarization, called the 31-mode. Typically, 33-mode actuators are used in axial devices and 31-mode actuators are used in bending devices. However, MFCs allow the more highly coupled 33-mode to be used in bending devices.

2.3 Immersed Cantilever Beam with Bimorph MFCs

2.3.1 Equation of Motion

The equation of motion for an Euler-Bernoulli bimorph cantilever subject to strain-rate and viscous damping that is excited by MFC actuators is given by [43]:

$$EI\frac{\partial^4 w(x,t)}{\partial x^4}+c_s I\frac{\partial^5 w(x,t)}{\partial x^4\partial t}+c_a\frac{\partial w(x,t)}{\partial t}+\mu\frac{\partial^2 w(x,t)}{\partial t^2}=-V(t)\frac{d^2\Gamma(x)}{dx^2} \qquad (2.3.1)$$

where $w(x,t)$ is the transverse displacement, c_sI is the strain-rate damping coefficient, c_a is viscous damping coefficient, μ is the mass per unit length of the beam, and $V(t)$ is the voltage applied to the MFC. The composite bending stiffness, EI, is a function of the elastic modulus and cross-sectional area for each layer within the composite beam. Figure 2.1 presents the cross-section for a beam with bimorph MFC actuators.

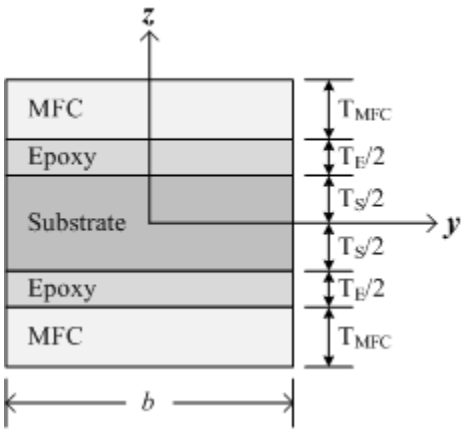

Figure 2.1 Cross-sectional area of a beam with bimorph MFC actuators.

This beam is classified as a composite beam because it is made from multiple materials that have been bonded together to form one structure. The cross-sectional area for a beam with bimorph

MFC actuators shown in Figure 2.1 is achieved by bonding MFC actuators to both sides of the substrate with epoxy, which results in a plane of symmetry at $y = 0$. This symmetry simplifies the calculation for the composite bending stiffness because the contribution from the bottom half of the beam is identical to the contribution from the top half of the beam. Accordingly, the composite bending stiffness is

$$EI = 2\left(E_S \int_{-b/2}^{b/2} \int_{0}^{T_S/2} z^2 dA + E_E \int_{-b/2}^{b/2} \int_{T_S/2}^{(T_S+T_E)/2} z^2 dA + E_{MFC} \int_{-b/2}^{b/2} \int_{(T_S+T_E)/2}^{(T_S+T_E)/2+T_{MFC}} z^2 dA \right) \qquad (2.3.2)$$

where E_s is the elastic modulus and $T_S/2$ is the thickness of the substrate layer, E_E is the elastic modulus and $T_E/2$ is the thickness of the epoxy layer, E_{MFC} is the elastic modulus and T_{MFC} is the thickness of the MFC, and b is the width of the beam. This expression reduces to

$$EI = \frac{b}{12}\left\{ E_S {T_S}^3 + E_E \left[\left(T_S + T_E \right)^3 - {T_S}^3 \right] + E_{MFC} \left[\left(T_S + T_E + 2T_{MFC} \right)^3 - \left(T_S + T_E \right)^3 \right] \right\} \qquad (2.3.3)$$

which shall be used to analyze Equation (2.3.1).

The expression $\Gamma(x)$ in Equation (2.3.1) accounts for the spatial distribution of the electric potential and is defined by

$$\Gamma\left(x\right) = \vartheta \sum_{i=1}^{N_e} \left\{ \left(1 + \frac{x - x_{i0}}{x_{i0} - x_{i1}} \right) \left[H\left(x - x_{i0}\right) - H\left(x - x_{i1}\right) \right] + \left(\frac{x - x_{i2}}{x_{i3} - x_{i2}} \right) \left[H\left(x - x_{i2}\right) - H\left(x - x_{i3}\right) \right] \right\} \qquad (2.3.4)$$

where ϑ is a coupling constant, x_{ij} represent geometric quantities, $H(x)$ is the Heaviside function, and N_e is the number of electrode pairs along the length of the beam, which may be approximated by $N_e \cong L_{act}/2(u_e+u_0)$. The parameter L_{act} is the active length of the cantilever beam, while u_e is the width of each electrode along the length of the beam and u_o is the width of each non-electroded region along the length of the beam. The geometry of the active region is described in detail in Figure 2.2.

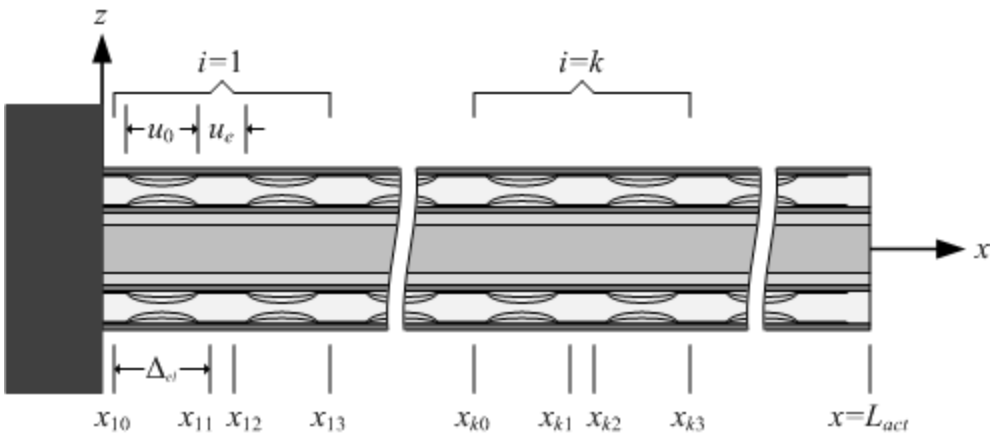

FIGURE 2.2 SCHEMATIC OF THE ACTIVE LENGTH OF A BIMORPH MFC BEAM.

The coupling constant, ϑ, in Equation (2.3.4) is given by

$$\vartheta = -\frac{e_{33} b_{pt} \left[\left(h_d - \alpha_p h_p \right)^2 - \left(h_c + \alpha_p h_p \right)^2 \right]}{2\Delta_{el}} \tag{2.3.5}$$

where e_{33} is the effective piezoelectric constant, α_p is an experimentally determined coefficient that reduces the effective thickness of the piezoceramic layer, b_{pt} is the width of the piezoelectric fibers, Δ_{el} is the effective electrode spacing, h_p is the thickness of the piezoelectric fibers, h_d is the distance from the neutral axis to the bottom of the piezoelectric layer and h_c is the distance from the neutral axis to the top of the piezoelectric layer.

Additional factors are introduced into Equation (2.3.1) to account for the non-trivial coupling between the solid and fluid domains that result from the swimming system operating in water. These factors address added mass and drag effects, which are typically ignored when a system vibrates in a low density, low viscosity fluid such as air. Blevins [49] defines added mass as the fluid force applied to a structure by the inertia of the fluid displaced by the structure as it moves. The inertia of the added mass has the same sign, frequency and phase as the inertia of the vibrating structure. Therefore, the added mass may be expressed as an added mass per unit length along the length of the beam. For an immersed cantilever beam, the force due to the added mass per unit length is

$$F_{AM} = \alpha \frac{\pi}{4} \rho_f b^2 \frac{\partial^2 w(x,t)}{\partial t^2} \tag{2.3.6}$$

where ρ_f is the density of the fluid in which the beam is immersed and b is the width of the beam. The parameter α, which is computed from tabular data presented in Blevins [49], adjusts the added mass appropriately for beams that have length to width ratios less than ten to one. For a beam that is long and narrow, the parameter α approaches one but as the width of the beam increases the parameter α becomes smaller. The drag force, unlike the force due to the added mass, is a nonlinear force that always opposes the motion of the beam. While in some instances it is possible to linearize the drag force, the classical drag expression shall be used for this analysis. Therefore, the drag force is

$$F_D = -\frac{1}{2}\rho_f S C_d \left|\frac{\partial w(x,t)}{\partial t}\right| \frac{\partial w(x,t)}{\partial t} \tag{2.3.7}$$

where S is the surface area exposed to the flow and C_d is the drag coefficient for that surface. The equation of motion for an immersed cantilever beam is obtained by inserting the expression for added mass in Equation (2.3.6) and the expression for the drag force in Equation (2.3.7) into Equation (2.3.1), which yields

$$\begin{aligned} EI\frac{\partial^4 w(x,t)}{\partial x^4} + c_s I\frac{\partial^5 w(x,t)}{\partial x^4 \partial t} + c_a\frac{\partial w(x,t)}{\partial t} + \frac{1}{2}\rho_f S C_d \left|\frac{\partial w(x,t)}{\partial t}\right| \frac{\partial w(x,t)}{\partial t} \\ + \mu\frac{\partial^2 w(x,t)}{\partial t^2} + \alpha\frac{\pi}{4}\rho_f b^2 \frac{\partial^2 w(x,t)}{\partial t^2} = -V(t)\frac{\partial^2 \Gamma(x)}{\partial x^2} \end{aligned} \tag{2.3.8}$$

2.3.2 Natural Frequencies and Mode Shapes

The undamped natural frequencies of the system are not dependant on external or internal damping; they are simply a function of the effective mass and stiffness. As such, the natural frequencies and mode shapes for an immersed cantilever beam are influenced by the inclusion of added mass and but they are not influenced by the inclusion of the drag force. Accordingly, the natural frequencies for an immersed cantilever beam will be significantly lower than those for a cantilever beam in air because the mass of the system has increased while the stiffness remains constant. The undamped natural frequencies for a clamped-free cantilever beam of length L, regardless of immersion media, are given as

$$\omega_r = \lambda_r^2 \sqrt{\frac{EI}{mL^4}} \tag{2.3.9}$$

where λ_r are the solutions to

$$1 + \cosh \lambda_r \cosh \lambda_r = 0 \tag{2.3.10}$$

and m is the effective mass per unit length of the system. When the system is operating in air, the effective mass per unit length is simply the mass per unit length of the beam, μ. However, when the system is immersed in a fluid, the effective mass per unit length is the mass per unit length of the beam plus the added mass per unit length from the fluid. Therefore, the natural frequencies for an immersed beam may be written as

$$\omega_r = \lambda_r^2 \sqrt{\frac{EI}{\left(\mu + \alpha \frac{\pi}{4} \rho_f b^2\right) L^4}} \tag{2.3.11}$$

The mass-normalized mode shapes express similar behavior when in the presence of an added mass. For a clamped-free cantilever beam, the mass-normalized mode shapes are

$$\phi_r(x) = \sqrt{\frac{1}{mL}} \left[\cosh \frac{\lambda_r}{L} x - \cos \frac{\lambda_r}{L} x - \sigma_r \left(\sinh \frac{\lambda_r}{L} x - \sin \frac{\lambda_r}{L} x \right) \right] \tag{2.3.12}$$

where

$$\sigma_r = \frac{\sinh \lambda_r - \sin \lambda_r}{\cosh \lambda_r + \cos \lambda_r} \tag{2.3.13}$$

Just as when examining the natural frequencies, the effective mass in Equation (2.3.12) depends on whether or not the beam the beam has been immersed in a fluid. Therefore, the effective mass per unit length is μ when the system operates in air and $\mu + \alpha \pi \rho_f b^2 / 4$ when immersed in a fluid. It should be noted that the mass normalized mode shapes satisfy the orthogonality conditions:

$$\int_0^L m\phi_s(x)\phi_r(x)\,dx = \delta_{rs}$$
$$\int_0^L EI\phi_s(x)\phi_1''''(x)\,dx = \omega_r^2\delta_{rs} \tag{2.3.14}$$

2.3.3 Modal Reduction of the Equation of Motion

Modal decomposition allows the system's response to be written as the summation of the responses produced by each of the system's modes. The solution to the equation of motion shown in Equation (2.3.8) is assumed to be

$$w(x,t) = \sum_{r=1}^{\infty}\phi_r(x)\eta_r(t) \tag{2.3.15}$$

where $\phi_r(x)$ is the mass normalized mode shape given by Equation (2.3.12) and $\eta_r(t)$ is the modal response for the r-th mode. The expression for the system's response may be truncated from the infinite series shown in Equation (2.3.15) to the response produced by a single mode when only considering excitation frequencies in the vicinity of the r-th mode. This is due to the fact that the response produced by the r-th mode will dominate the infinite series when excited at a frequency near the r-th mode. Therefore, the system's response in the vicinity of the first mode may be approximated by

$$w(x,t) = \phi_1(x)\eta_1(t) \tag{2.3.16}$$

where $\phi_1(x)$ is the mass normalized mode shape and $\eta_1(t)$ is the modal response for the mode for the first mode. Inserting Equation (2.3.16) into the equation of motion yields

$$\begin{aligned} &EI\phi_1''''(x)\eta_1(t) + c_s I\phi_1''''(x)\dot{\eta}_1(t) + c_a\phi_1(x)\dot{\eta}_1(t) \\ &\quad + \frac{1}{2}\rho_f SC_d\left|\phi_1(x)\dot{\eta}_1(t)\right|\phi_1(x)\dot{\eta}_1(t) + m\phi_1(x)\ddot{\eta}_1(t) = -V(t)\Gamma''(x) \end{aligned} \tag{2.3.17}$$

Equation (2.3.17) is premultiplied by $\phi_1(x)$ and integrated over length of beam while noting the orthogonality conditions in Equation (2.3.14) to produce

$$\ddot{\eta}_1(t)+\left(\frac{c_s I\omega_1^2}{EI}+\frac{c_a}{m}\right)\dot{\eta}_1(t)+\frac{1}{2}\rho_f SC_d\left|\dot{\eta}_1(t)\right|\dot{\eta}_1(t)\int_0^L\left|\phi_1(x)\right|\phi_1^2(x)\,dx + \omega_1^2\eta_1(t)=-V(t)\int_0^L\Gamma''(x)\phi_1(x)\,dx \tag{2.3.18}$$

For simplicity, (2.3.18) is reduced to more familiar terms

$$\ddot{\eta}_1(t)+2\zeta_1\omega_1\dot{\eta}_1(t)+\omega_1^2\eta_1(t)+\frac{1}{2}\rho_f SC_d D_1\left|\dot{\eta}_1(t)\right|\dot{\eta}_1(t)=-\chi_1 V(t) \tag{2.3.19}$$

where ζ_1 is the modal damping ratio given by

$$\zeta_1=\frac{c_s I\omega_1}{2EI}+\frac{c_a}{2m\omega_1} \tag{2.3.20}$$

D_1 is the modal drag coefficient given by

$$D_1=\int_0^L\left|\phi_1(x)\right|\phi_1^2(x)\,dx \tag{2.3.21}$$

and χ_1 is the piezoelectric forcing coefficient given by

$$\chi_1=\int_0^L\Gamma''(x)\phi_1(x)\,dx \tag{2.3.22}$$

The governing differential equation that is presented as Equation (2.3.19) is nonlinear due to the incorporation of drag. Nonlinear differential equations of this form do not have analytical solutions. Consequently, solutions to the modal response model must be obtained by employing a numerical approach in the software package, such as MATLAB.

An imprecise approximation can be applied to linearize the drag term in order to linearize the differential equation that governs the modal response. This linearization is not sufficiently accurate to be considered when determining the modal response of the system, although it may be used to generate an approximate Frequency Response Function (FRF) for the composite beam as it vibrates in water. This approximate FRF will be compared to experimental data to verify the added mass assumption presented in Section 2.3.1. Therefore, the linearized differential equation that governs the system's modal response in water and is only used to generate an approximate FRF is

$$\ddot{\eta}_1(t) + 2\left(\zeta_r + \zeta_{f,1}\right)\omega_1\dot{\eta}_1(t) + \omega_r^2\eta_1(t) = -\chi_1 V(t) \tag{2.3.23}$$

where $\zeta_{f,1}$ is the linearized fluidic damping ratio for the first mode, which accounts for the composite beam being immersed in a slow moving fluid and vibrating with small amplitude. The analytical solution to Equation (2.3.23) is

$$\eta_1(t) = \frac{-\chi_1}{\omega_1^2 - \omega^2 + i2\left(\zeta_1 + \zeta_{f,1}\right)\omega_1\omega} V(t) \tag{2.3.24}$$

The modal response is differentiated and multiplied by the mass normalized mode shape to produce the velocity transfer function for the system when excited at frequencies near the first mode and while operating in water

$$\frac{\dot{w}(x,t)}{V(t)} = \frac{-i\omega\chi_1\phi_1(x)}{\omega_1^2 - \omega^2 + i2\left(\zeta_1 + \zeta_{f,1}\right)\omega_1\omega} \tag{2.3.25}$$

While the modal damping ratio and piezoelectric forcing coefficient can be determined analytically using Equations (2.3.20) and (2.3.22), these parameters are more easily obtained directly from experimental data. Similarly, the modal fluidic damping ratio shall be obtained by performing system identification.

Rather than attempt to identify these three parameters from the immersed FRF, the modal damping ratio and piezoelectric forcing coefficient can easily be determined from the FRF for the system as it operates in air. This is because these parameters are inherent to the structure of the device and not dependant on the fluid in which they are immersed. The FRF for the system in air is identical to that for the system in water when the modal fluidic damping term is neglected

$$\frac{\dot{w}(x,t)}{V(t)} = \frac{-i\omega\chi_1\phi_1(x)}{\omega_1^2 - \omega^2 + i2\zeta_1\omega_1\omega} \tag{2.3.26}$$

Once these coefficients have been determined, the FRF generated for the composite beam in water can be compared with experimental data to verify the added mass assumption.

2.4 MODELING HYDRODYNAMIC THRUST

A model for the hydrodynamic thrust produced by a fin, as well the swimming speed of a vehicle with an affixed fin, has been developed by Zhang and Liu [16]. Their model is based on three assumptions: the fluid is incompressible and the disturbance flow is negligible, the thickness of the fin is negligible when compared to its length, and the vehicle's mean steady-state swim speed is low and constant. Thrust is determined from analysis on the normal and tangential forces that arise along the length of the fin as it deflects in a fluid. These vectors as well as the angle of deflection, θ, are shown for a cantilever beam in Figure 2.3.

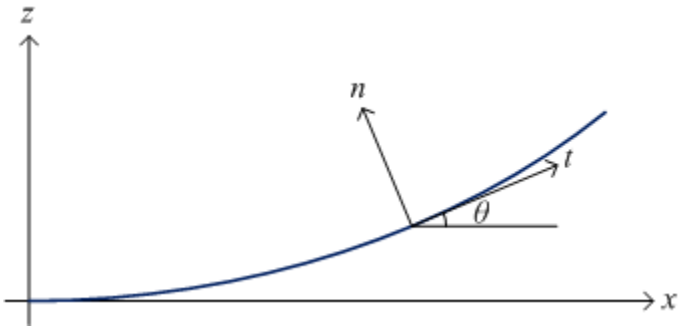

FIGURE 2.3 NORMAL AND TANGENTIAL VECTORS ALONG BEAM LENGTH.

The vibration amplitude of the beam is sufficiently small enough for the classical small angle approximations $\theta = \sin\theta = \tan\theta = dz/dx$ to hold.

The normal and tangential forces that arise along the length of the beam are due to hydrodynamic drag, which indicates they are of the form

$$\begin{aligned} \boldsymbol{F}_n &= -\frac{1}{2} C_n \rho_f S \boldsymbol{V}_n \left\| \boldsymbol{V}_n \right\| \\ \boldsymbol{F}_t &= -\frac{1}{2} C_t \rho_f S \boldsymbol{V}_t \left\| \boldsymbol{V}_t \right\| \end{aligned} \tag{2.4.1}$$

where C_n and C_t are the normal and tangential drag coefficients and V_n and V_t are the normal and tangential beam velocities. While both drag coefficients depend heavily on the Reynolds number, the normal drag coefficient may be approximated as $C_n = 1.2$ by assuming the flow is low and stable. However, the Reynolds number must be determined to obtain the drag

coefficient in the tangential direction. The Reynolds number, which varies along the length of the beam, is given as

$$\mathrm{Re} = \frac{x}{\nu}\frac{\partial w(x,t)}{\partial t} \tag{2.4.2}$$

where ν is the kinematic viscosity of the fluid, x is the position along the length of the beam, and $w(x,t)$ is the transverse displacement of the beam. When the $\mathrm{Re} < 5 \times 10^5$, the tangential drag coefficient may be approximated as

$$C_t = 1.372\sqrt{\frac{1}{\mathrm{Re}}} \tag{2.4.3}$$

which varies as a function of both position and time due to the motion of the beam.

The forces along the length of the beam are obtained by first determining the normal and tangential velocities. These velocities, in the absolute coordinates $\hat{x}$ and $\hat{z}$, are defined as

$$\begin{aligned} V_x &= U \\ V_z &= \frac{\partial w(x,t)}{\partial t} \end{aligned} \tag{2.4.4}$$

where U is the velocity of the fluid flow that were to result if the beam were placed into a flowing stream. These velocities are converted into the normal and tangential directions by applying a coordinate transformation:

$$\begin{aligned} V_n &= -V_x \sin\theta + V_z \cos\theta \\ V_t &= V_x \cos\theta + V_z \sin\theta \end{aligned} \tag{2.4.5}$$

These velocities are then used to determine the fluid forces along a differential element of the beam in the normal and tangential coordinates, which are

$$\begin{aligned} dF_n &= -\frac{1}{2} C_n \rho_f V_n \|V_n\| ds \\ dF_t &= -\frac{1}{2} C_t \rho_f V_t \|V_t\| ds \end{aligned} \tag{2.4.6}$$

where ds is a differential beam element. The length of the differential element is converted into the absolute coordinate system by noting

$$ds = b\frac{dx}{\cos\theta} \tag{2.4.7}$$

Applying Equation (2.4.7) to Equation (2.4.6) and performing an additional coordinate transformation brings the differential forces into the absolute coordinate system:

$$\begin{aligned} dF_x &= \frac{1}{2}\rho_f\left(C_n V_n\|V_n\|\tan\theta - C_t V_t\|V_t\|\right)dx \\ dF_z &= -\frac{1}{2}\rho_f\left(C_n V_n\|V_n\| + C_t V_t\|V_t\|\tan\theta\right)dx \end{aligned} \tag{2.4.8}$$

Integration along the surface of the beam provides the total force in the $\hat{x}$ and $\hat{z}$ directions

$$\begin{aligned} F_x &= \int_0^L \frac{1}{2}\rho_f b\left(C_n V_n\|V_n\|\tan\theta - C_t V_t\|V_t\|\right)dx \\ F_z &= \int_0^L -\frac{1}{2}\rho_f b\left(C_n V_n\|V_n\| + C_t V_t\|V_t\|\tan\theta\right)dx \end{aligned} \tag{2.4.9}$$

Since force along the $\hat{z}$ direction has little influence on the system, the mean thrust acting along the system per cycle is

$$\overline{F} = \frac{\int_0^T F_x dt}{T} \tag{2.4.10}$$

where T is the period of the excitation signal. Due to the way this model has been derived positive thrust corresponds to the device swimming backwards while negative thrust corresponds to the device swimming forward. Additionally, the mean swimming speed of a vehicle with this propulsion system is obtained by setting the mean thrust equal to the drag force acting on the vehicle:

$$v = \operatorname{sgn}\left(\overline{F}\right)\sqrt{\frac{2\left|\overline{F}\right|}{\rho_f C_v S_v}} \tag{2.4.11}$$

where C_v is the drag coefficient and S_v is the exposed surface area for the vehicle.

2.5 CHAPTER SUMMARY

This chapter aimed to develop a model to predict the amount of thrust produced by a composite cantilever beam with bimorph MFC actuators that vibrates in water. The foundation necessary to accomplish this task is presented as a review of classical Euler-Bernoulli beam theory as well as an introduction to linear piezoelectricity. A model for the vibration of the composite beam in air is presented that combines Euler-Bernoulli beam theory with linear piezoelectricity. Rudimentary fluid mechanics are incorporated into this model to predict the behavior of the composite beam as it vibrates in water. The resultant motion is then subjected to a model originally developed by Zhang and Liu [16] that predicts the thrust produced by a vibrating fin. These results are then expanded to predict the swimming velocity achievable by a vehicle using this system.

3 EXPERIMENTAL TESTING & RESULTS

3.1 EXPERIMENTATION OVERVIEW

The experimental research objective is to validate the dynamical models derived in Chapter 2, which present hydrodynamic thrust and the associated swimming velocity as functions of the voltage applied to the MFC actuators. Model verification is attempted by performing two distinct, yet ultimately related, experiments. These experiments are designed to measure the system's FRF in both air and water as well as measure the thrust produced for several different beam configurations with various excitation frequencies and supply voltages.

Initial experimentation aimed to address the most common question one is asked when discussing a vibratory system: "What are the natural frequencies?" The natural frequencies are obtained by measuring the FRF that relates the swimming system's tip velocity to the excitation frequency while the system operates in air as well as water. Measurements are performed in air and water to verify that the added mass assumption included in the dynamical model is correct. The second round of experimentation addressed how much thrust is produced over the frequency range from 5-20Hz, which encompasses the first mode for all systems, for several excitation voltages. This data is compared to the hydrodynamic thrust model in an attempt to verify and to improve upon the hydrodynamic thrust model.

3.1.1 FABRICATION OF BIMORPH MFC CANTILEVER BEAMS

Four bimorph MFC cantilever beams are fabricated for experimental testing. The bimorph beams are made from two MFC actuators that are either bonded together or bonded to a substrate material with 3M DP-460 epoxy. The epoxy is allowed to cure for 6 hours within a vacuum to form a thin, uniform bond layer. Two beams, one with and one without a 0.001" thick stainless steel substrate are made from each MFC actuators being considered. The actuators used during the experiments are M-8528-P1 and M-8507-P1 d_{33} effect MFC actuators by Smart Material Corporation. The active area on the M-8528-P1 and M-8507-P1 is 85×28mm

and 85×7mm. The fully fabricated composite cantilever beams have the clamped dimensions presented in Table 3-1

TABLE 3-1 DIMENSIONS OF MANUFACTURED COMPOSITE BEAMS.

MFC	Substrate	L [mm]	b [mm]	T [mm]	T_S [mm]	T_E [mm]
M-8528-P1	--	91.5	40.4	0.69	0	0.09
M-8528-P1	Stainless Steel	89.6	40.4	0.79	0.0254	0.165
M-8507-P1	--	83.2	16.2	0.63	0	0.03
M-8507-P1	Stainless Steel	84.3	16.2	0.69	0.0254	0.065

Table 3-1 also presents the epoxy layer thickness, which can vary rather significantly during the manufacture process. Nevertheless, in both cases the epoxy layer thickness approximately doubles with the inclusion of a substrate, which is to be expected. Representative devices using the M-8528-P1 and M-8507-P1 MFC actuators are shown in Figure 3.1.

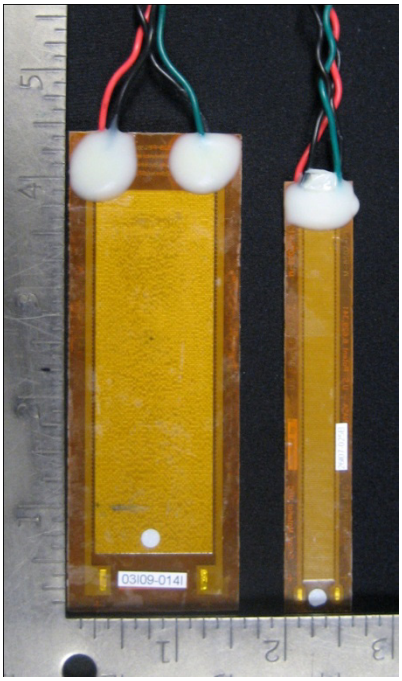

FIGURE 3.1 REPRESENTATIVE SWIMMING SYSTEMS USING M-8528-P1 AND M-8507-P1 MFCS.

A thick layer of epoxy applied to the electrodes on the MFC actuators shown Figure 3.1 to provide insulation. This insulation layer is allowed to fully cure for one week to ensure the electrodes are properly insulated before conducting any experimental testing. The mass added by the insulation layer does not influence vibration characteristics because the beams are clamped on their active area slightly beyond the insulation layer.

3.2 Frequency Response Functions

3.2.1 Experimental Setups

Two nearly identical experimental setups are employed to measure the FRFs of various composite beams in air and water. The difference between these experimental setups rests with the manner in which the cantilever beam is mounted. When measuring FRFs in air, the cantilever beam is mounted via a vice clamp onto a Newport ST Series Smart Table with Auto-Tune Damping vibration isolation table. Similarly, when measuring FRFs in water, the cantilever beam is affixed via hand clamps to an apparatus that is ultimately connected to a concrete vibration isolation block. The schematic shown in Figure 3.2 displays the five components that comprise the FRF measurement system used for both air and water measurements.

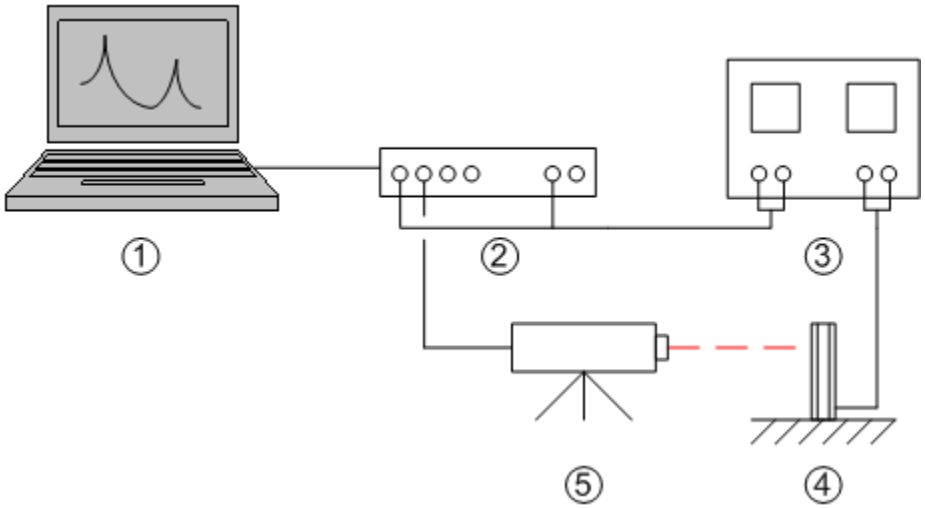

Figure 3.2 Schematic of the Frequency Response Function measuring system.

The measurement system employs a laptop computer (1) that is connected to a DSP Technology, Inc. SigLab Model 20-42 dynamic signal analyzer (2), which integrates with MATLAB running on the laptop. A random burst signal generated within the MATLAB based interface is output through SigLab's Output Channel 1. The output signal is routed into SigLab's Input Channel 1 as well as into a HP 6826A Bipolar Power Supply and Amplifier (3). The amplifier amplifies the signal by a factor of ten before it is routed as an input into one of the MFC actuators on the composite beam (4), which causes the beam to vibrate. A Polytec PDV 100 laser vibrometer (5) measures the beam's tip velocity while it is excited by the random signal.

The measurement signal produced by the laser vibrometer is routed into Input Channel 2 on the SigLab. This signal is analyzed in conjunction with the excitation signal to produce a FRF.

3.2.1.1 Experimental Setup for FRF Measurements in Air

The experimental setup used to measure the FRF of a composite cantilever beam while it vibrates in air is built upon the schematic shown in Figure 3.2 and presented in Figure 3.3.

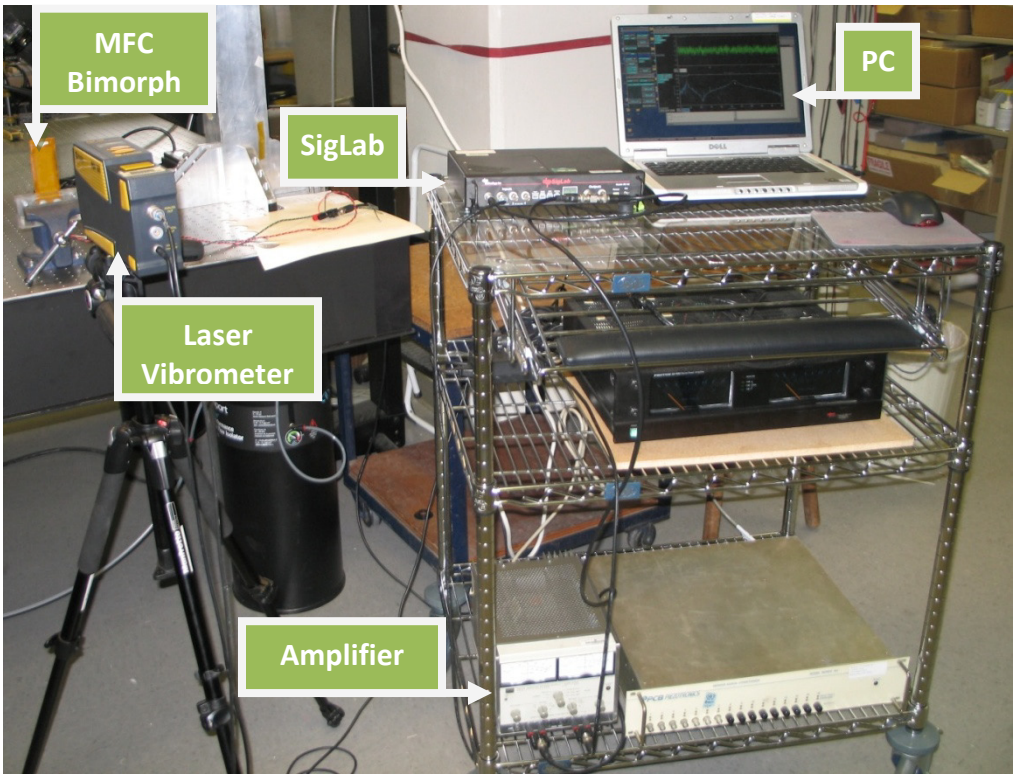

Figure 3.3 FRF measurement system for air based measurements.

The components in Figure 3.3 match those presented in Figure 3.2 with a few additions. The clamping mechanism is mounted on the vibration isolation table to minimize the vibration that results from working in a populated, third floor lab. A close-up image showing the clamping mechanism that supports the cantilever beam is presented in Figure 3.4.

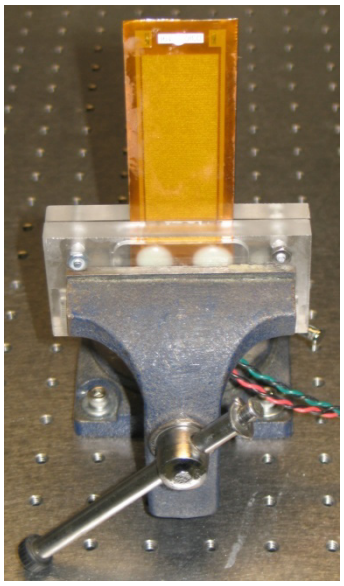

FIGURE 3.4 CLAMPING MECHANISM USED IN AIR BASED FRF MEASUREMENTS.

The clamping mechanism consists of an acrylic housing that is compressed inside a vice clamp to provide the fixed boundary condition. The vice clamp, as previously mentioned, is attached to the vibration isolation table.

3.2.1.2 EXPERIMENTAL SETUP FOR FRF MEASUREMENTS IN WATER

The experimental setup used to measure the FRF of a composite beam while it vibrates in water is virtually identical to that used when the composite beam vibrates in air. The main difference arises from the fact that the beam is fully immersed in water. Consequently, an alternate clamping mechanism is employed because the clamping mechanism used to support the cantilever beam in air cannot be directly mounted within an aquarium. Unfortunately, the water clamping mechanism is less robust than its air counterpart, which introduces noise into the system's FRF. The full FRF measurement system for an immersed cantilever beam is shown in Figure 3.5.

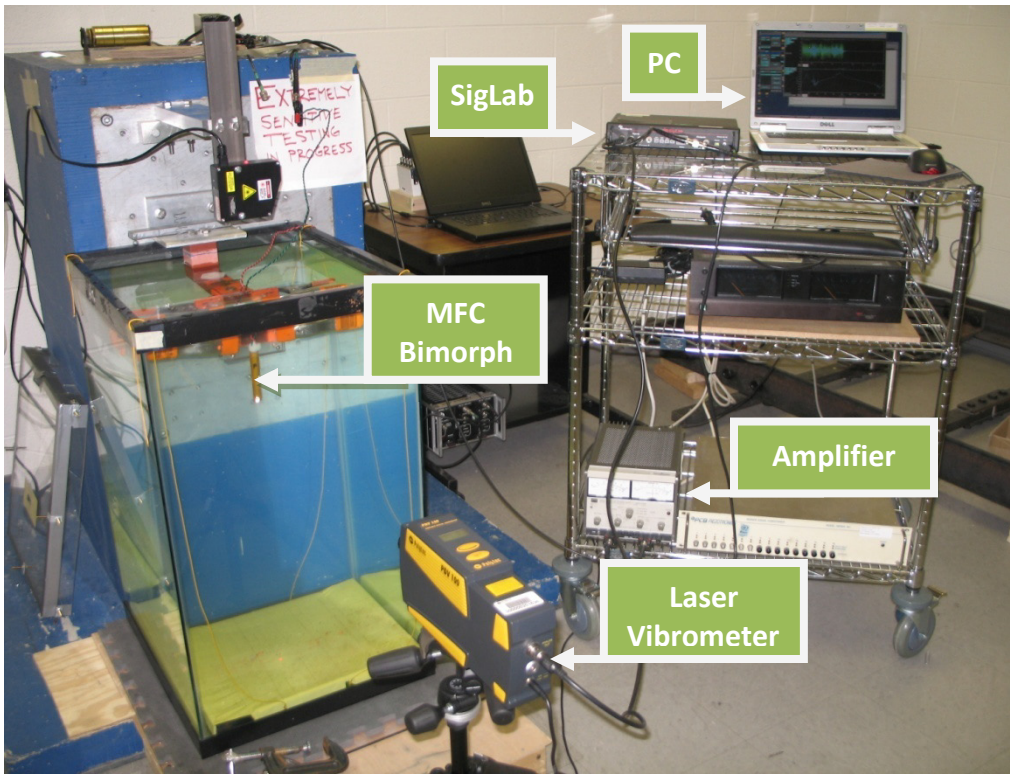

FIGURE 3.5 FRF MEASUREMENT SYSTEM FOR WATER BASED MEASUREMENTS.

The clamping mechanism shown in Figure 3.5 is mounted onto an arm that extends from a concrete vibration isolation block into a 45 gallon water tank. A close-up of the clamping mechanism is presented in Figure 3.6.

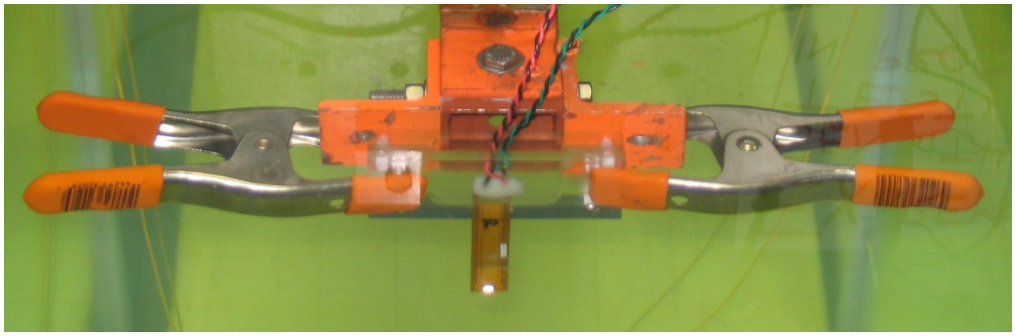

FIGURE 3.6 CLAMPING MECHANISM USED IN WATER BASED FRF MEASUREMENTS.

The bimorph MFC beam is placed within the same acrylic housing used while performing air based FRF measurements. However, rather than using a vice clamp, the housing is mounted onto the extensional arm that stems from the vibration isolation block via hand clamps. This mechanism provides sufficient, though less robust, results than the mechanism used to measure

FRFs because the hand clamps do not provide a uniform compressive force along the length of the housing.

3.2.2 FRF Experimental Results

Experimental data is collected in both media for the four composite cantilever beams being tested. As previously mentioned, these beams are made from bimorph M-8528-P1 and M-8507-P1 MFC actuators that have been bonded to either a 0.001" thick stainless steel substrate or directly together with 3M DP-460 epoxy. The FRF measurements are performed near the base of the device.

3.2.2.1 FRFs for M-8528-P1 Based Systems

The experimental apparatuses discussed in Section 3.2.1 are used to generate the velocity FRFs for the composite cantilever beams that have M-8528-P1 MFCs while they operate in both air and water. The results of these analyses produce the air based FRF shown in Figure 3.7 and the water based FRF shown in Figure 3.8.

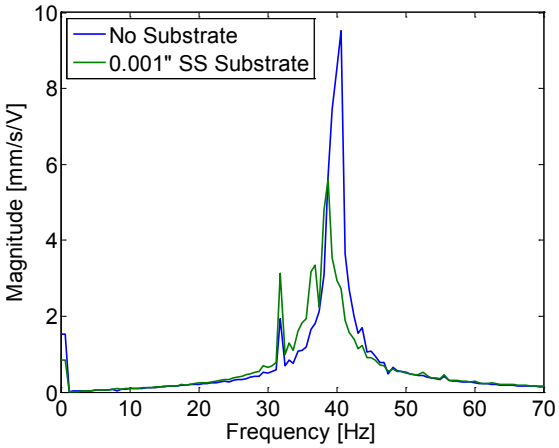

Figure 3.7 Air FRFs for beams with M-8528-P1 MFCs.

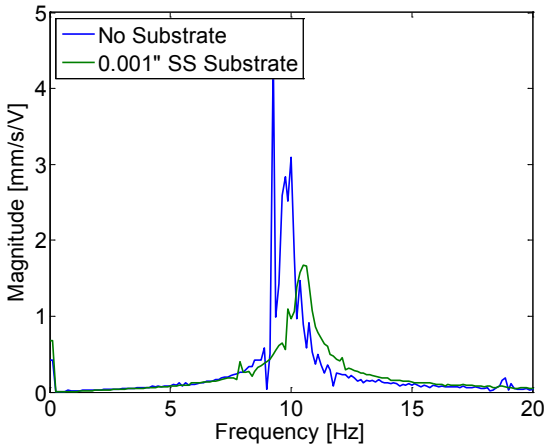

Figure 3.8 Water FRFs for beams with M-8528-P1 MFCs.

The composite beam with a substrate does not produce as significant tip velocities as the composite beam without a substrate. As expected, immersing the composite beams in water significantly reduces their natural frequencies due to the added mass of the water. Moreover,

the tip velocities of the composite beams are also significantly decreased by being immersed in water.

3.2.2.2 FRFs for M-8507-P1 Based Systems

The same analyses are applied to composite cantilever beams with M-8507-P1 MFCs that operate in both air and water. The results of these analyses produce the air based FRF shown in Figure 3.9 and the water based FRF shown in Figure 3.10.

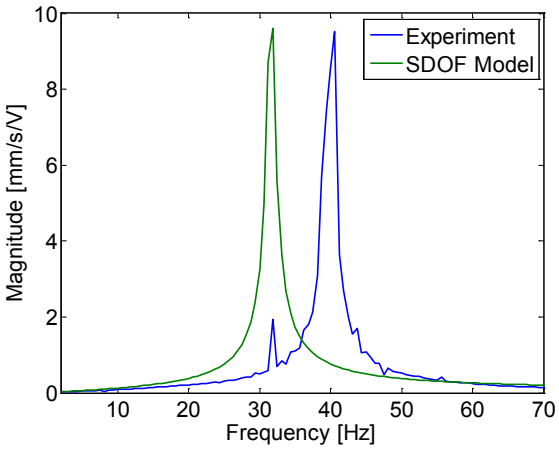

Figure 3.9 Air FRFs for beams with M-8507-P1 MFCs.

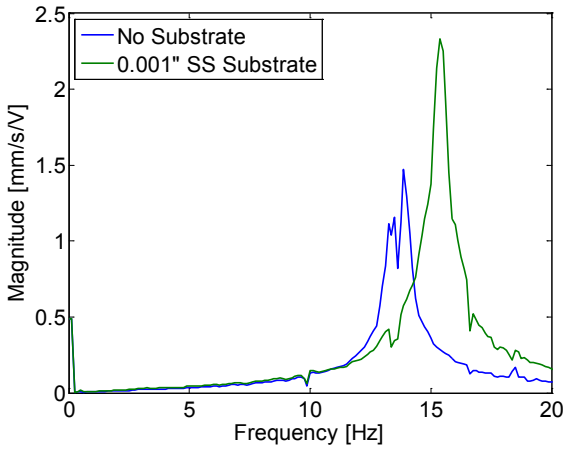

Figure 3.10 Water FRFs for beams with M-8507-P1 MFCs.

Interestingly, when the M-8507-P1 actuator is used, the tip velocities of the composite beam with a substrate layer are greater than those without the substrate layer, which is the exact as observed when the M8528-P1 actuators are used. This occurs as a result of variations in material damping between the composite beams. Material damping changes as a function of substrate layer thickness, epoxy layer thickness, and any pre-strain that may be within the system due to the manner in which the beams bond to the substrate or one another. Nevertheless, immersing the cantilever beams in water once again significantly reduces the natural frequencies of the system as well the tip velocities.

3.2.3 Comparison to Analytical Model

The experimentally observed FRF are compared to the analytically determined FRFs that are based on Equations (2.3.25) and (2.3.26) presented in Section 2.3.3. The modal damping

ratio, fluidic damping ratio, and piezoelectric forcing coefficient have been determined experimentally through system identification.

3.2.3.1 M-8528-P1 Based Systems

The FRFs for a composite cantilever beam with bimorph M-8528-P1 MFC actuators and no substrate while vibrating in air and while immersed in water are shown in Figure 3.11 and Figure 3.12, respectively.

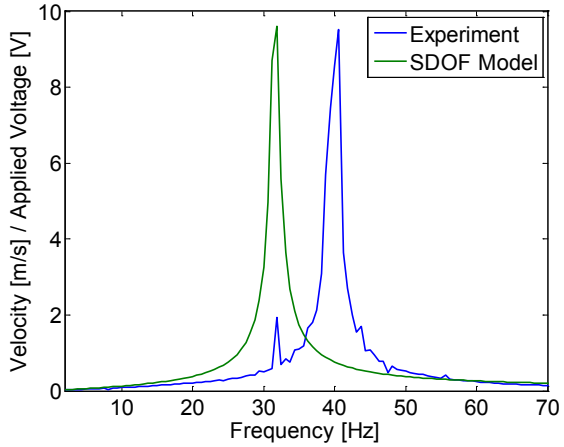

Figure 3.11 Air FRF for M-8528-P1 beam, no substrate.

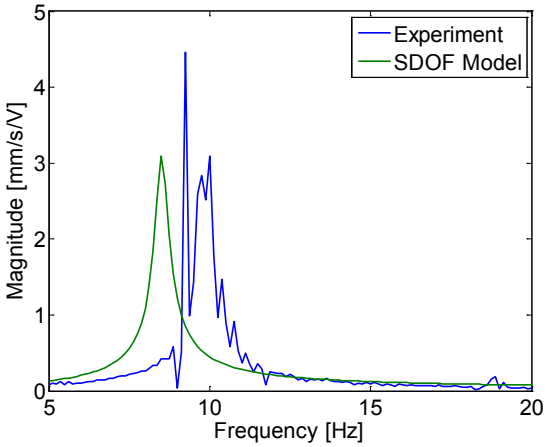

Figure 3.12 Water FRF for M-8528-P1 beam, no substrate.

These FRFs have been generated using values for the modal damping ratio, modal fluidic damping ratio, and piezoelectric forcing coefficient that were determined experimentally via system identification. A scaling coefficient, κ, is employed to scale the analytical velocity FRF for the immersed case to match the experimentally observed velocity FRF. Effectively, the scaling coefficient accounts for the reduced motion that occurs as a result of the device being immersed. These experimental parameters are provided in Table 3-2.

Table 3-2 Experimental parameters for beam with M-8528-P1 MFCs, no substrate.

χ_1	ζ_1	$\zeta_{1,f}$	κ
0.021	0.017	0.0065	0.405

The analytical model predicts significantly lower natural frequencies than those observed experimentally when using the parameters shown in Table 3-2. These results are summarized in Table 3-3, which presents the experimentally and analytically determined natural frequencies as well as the percentage error between the experiments and models.

TABLE 3-3 NATURAL FREQUENCIES FOR BEAM WITH M-8528-P1 MFCS, NO SUBSTRATE.

	$\omega_{1,Experimental}$ [Hz]	$\omega_{1,Model}$ [Hz]	Error [%]
Air	40.63	31.62	22.2
Water	9.875	8.518	13.7

These error levels are well beyond what is typically deemed acceptable for a composite beam vibrating in air. This can be the result of issues with the clamped boundary, variations in epoxy layer thickness that cause non-uniform beam thickness, and pre-strain in the composite beam that causes a small amount of warping.

The FRFs for a composite cantilever beam with bimorph M-8528-P1 MFC actuators and a 0.001" thick stainless steel substrate while vibrating in air and while immersed in water are shown in Figure 3.13 and Figure 3.14, respectively.

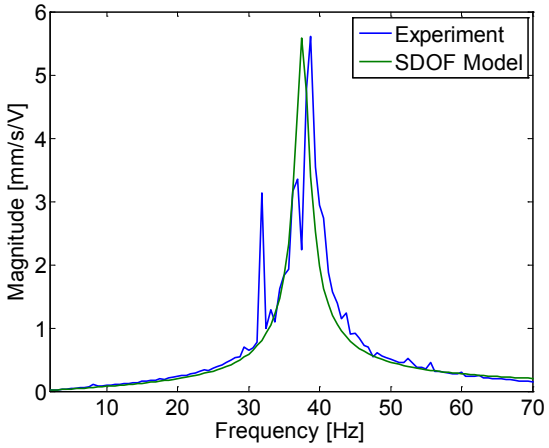

FIGURE 3.13 AIR FRF FOR M-8528-P1 BEAM, 0.001" S.S. SUBSTRATE.

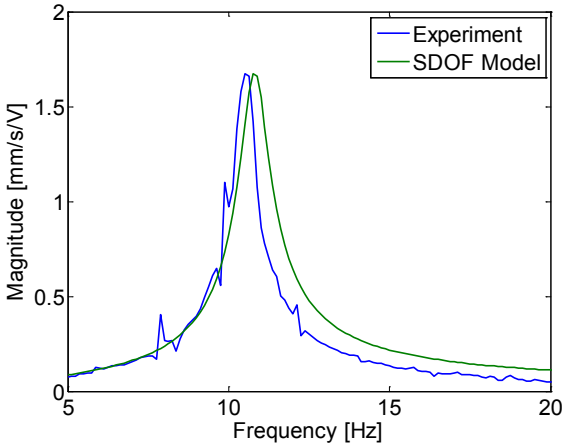

FIGURE 3.14 WATER FRF FOR M-8528-P1 BEAM, 0.001" S.S. SUBSTRATE.

The parameters associated with these models are provided in Table 3-4.

TABLE 3-4 EXPERIMENTAL PARAMETERS FOR BEAM WITH M-8528-P1 MFCS, 0.001" S.S. SUBSTRATE.

χ_1	ζ_1	$\zeta_{1,f}$	κ
0.02	0.024	0.0195	0.545

The responses predicted by the analytical models appear to agree rather well with the experimental data for both the air and water based experiments. The experimental and analytical natural frequencies as well as the percentage error between the experiments and models shown presented in Table 3-5.

TABLE 3-5 NATURAL FREQUENCIES BEAM WITH M-8528-P1 MFCS, 0.001" S.S. SUBSTRATE.

	$\omega_{1,Experimental}$ [Hz]	$\omega_{1,Model}$ [Hz]	Error [%]
Air	38.75	37.55	3.1
Water	10.63	10.80	1.6

The error for the first natural frequency when the system is in water is less than predicted when the system operates in air because the frequency predicted by the model in water is slightly higher than that observed experimentally. Overall, however, these error levels are fairly small which indicates the high level of agreement between the models and experimental results. The accuracy of these results further stresses that issues with the clamped boundary, variations in epoxy layer thickness, and/or warping likely contributed to the high amount of error observed for M-8528-P1 composite beam with no substrate.

3.2.3.2 M-8507-P1 BASED SYSTEMS

The FRFs for a composite cantilever beam with bimorph M-8507-P1 MFC actuators and no substrate while vibrating in air and while immersed in water are shown Figure 3.15 and Figure 3.16, respectively.

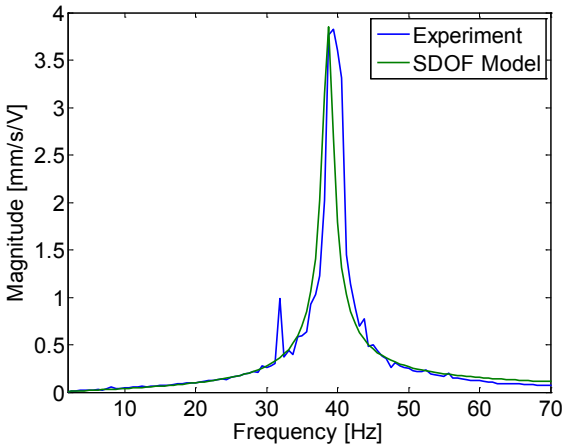

FIGURE 3.15 AIR FRF FOR M-8507-P1 BEAM, NO SUBSTRATE.

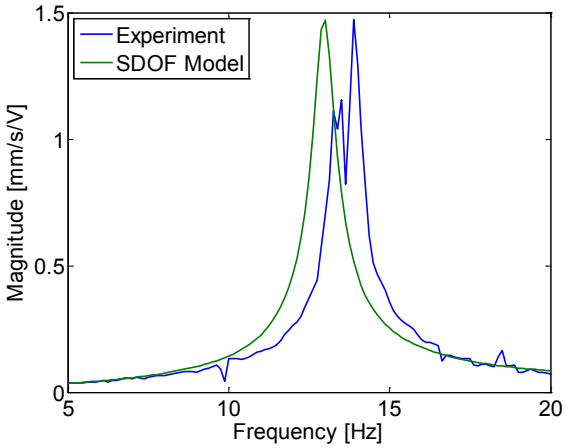

FIGURE 3.16 WATER FRF FOR M-8507-P1 BEAM, NO SUBSTRATE.

The parameters associated with these models are provided in Table 3-6.

TABLE 3-6 EXPERIMENTAL PARAMETERS FOR BEAM WITH M-8507-P1 MFCS, NO SUBSTRATE.

χ_1	ζ_1	$\zeta_{1,f}$	κ
0.005	0.018	0.0075	0.537

Once again, the responses predicted by the analytical models agree rather well with the experimental data for both the air and water based experiments. The experimental and analytical natural frequencies as well as the percentage error between the experiments and models shown presented in Table 3-7.

TABLE 3-7 NATURAL FREQUENCIES FOR BEAM WITH M-8507-P1 MFCS, NO SUBSTRATE.

	$\omega_{1,Experimental}$ [Hz]	$\omega_{1,Model}$ [Hz]	Error [%]
Air	39.38	38.63	1.9
Water	13.88	12.96	6.6

The errors shown in Table 3-7 are low for both the air and water based experiments, further stressing the high level of agreement between the analytical models and experimental results.

The FRFs for a composite cantilever beam with bimorph M-8507-P1 MFC actuators and a 0.001" thick stainless steel substrate while vibrating in air and while immersed in water are shown in Figure 3.17 and Figure 3.18, respectively.

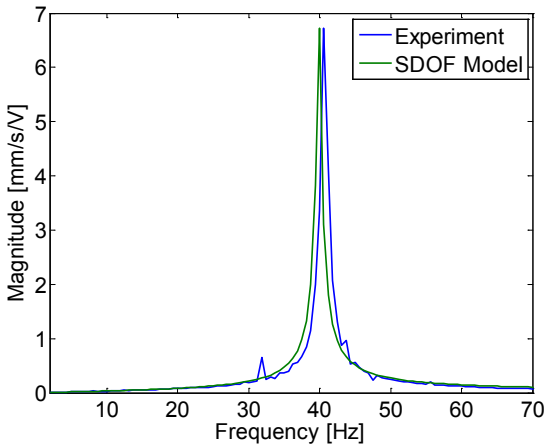

FIGURE 3.17 AIR FRF FOR M-8507-P1 BEAM, 0.001" S.S. SUBSTRATE.

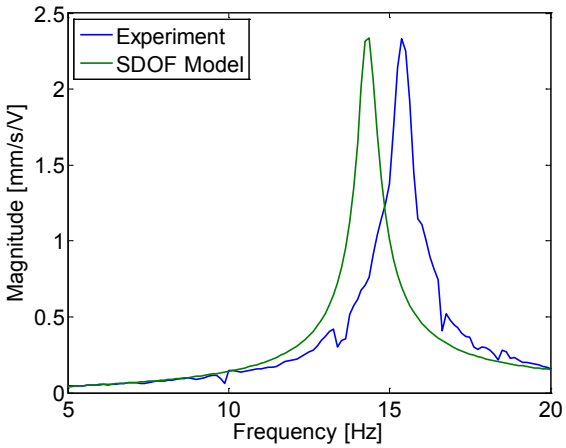

FIGURE 3.18 WATER FRF FOR M-8507-P1 BEAM, 0.001" S.S. SUBSTRATE.

The parameters associated with these models are provided in Table 3-8.

TABLE 3-8 EXPERIMENTAL PARAMETERS FOR BEAM WITH M-8507-P1 MFCS, 0.001" S.S. SUBSTRATE.

χ_1	ζ_1	$\zeta_{1,f}$	κ
0.005	0.0089	0.013	0.842

Yet again, the responses predicted by the analytical models agree rather well with the experimental data for both the air and water based experiments. The experimental and

analytical natural frequencies as well as the percentage error between the experiments and models shown presented in Table 3-9.

TABLE 3-9 NATURAL FREQUENCIES FOR BEAM WITH M-8507-P1 MFCS, 0.001" S.S. SUBSTRATE.

	$\omega_{1,Experimental}$ [Hz]	$\omega_{1,Model}$ [Hz]	Error [%]
Air	40.63	39.91	1.8
Water	15.38	14.32	6.9

As with the M-8507-P1 experiment without a substrate and the M-8528-P1 experiment with a 0.001" thick stainless steel substrate, the errors presented are again fairly low and highlight the level of agreement between the analytical models and experimental results.

3.2.4 SUMMARY OF THE FRF RESULTS

While the analytical models did not agree well when analyzing the composite beam with bimorph M-8528-P1 MFCs and no substrate, it did perform reasonably well when analyzing the remaining systems. The largest error observed while predicting a system's natural frequency in water was 6.9%, which is rather small when considering the fact that these complex, nonlinear systems have been approximated by simple, single mode models. This relatively small error indicates the added mass assumption predicts the natural frequencies of an immersed beam reasonably well and fine tuning the added mass term will bring these results more in line with the experimentally determined values. However, the simplifications to the model did not accurately predict the magnitude of the system's response. This was only attained by applying a non-physical scaling coefficient to each system to account for the reduced motion in the fluid.

3.3 THRUST EXPERIMENTS

3.3.1 EXPERIMENTAL SETUP

Thrust measurements are obtained indirectly from a highly specialized, as well as highly sensitive, experimental test platform that is capable of resolving thrusts smaller than one milli Newton. There are eight main components to the platform, which is controlled by a custom LabVIEW program. A schematic for the system is shown in Figure 3.19.

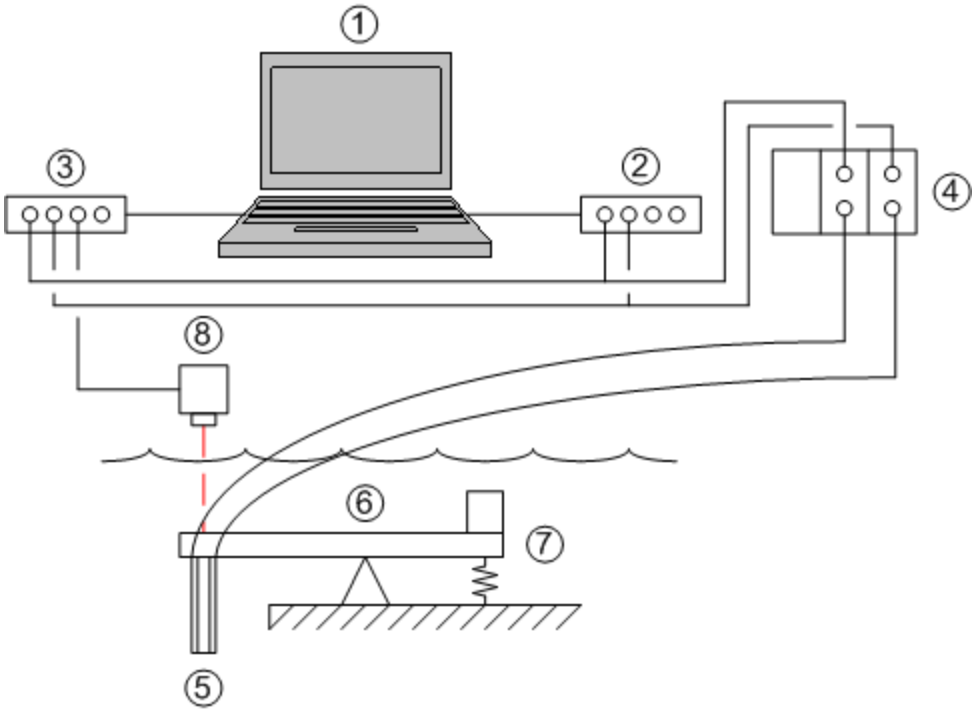

FIGURE 3.19 SCHEMATIC OF THE HYDRODYNAMIC THRUST MEASURING SYSTEM.

A laptop computer running a custom LabVIEW program (1) is connected to a National Instruments NI-9263 analog voltage output card (2) and a National Instruments NI-9215 simultaneous analog input card (3) through National Instruments NI-9162 USB carriers. Both National Instruments I/O cards have 4-channels with 16-bit resolution. Additionally, the dynamic range for each card is customized to maximize resolution. The LabVIEW program running on the laptop generates two signals, one for each MFC on the composite beam, that are output by Channels 0 and 1 on the analog output card. Each output signal is routed to the matching channel on the analog input card and to a Trek 50/750 high voltage amplifier (4). The amplifier applies a gain of 300 to the input signals before they are routed to the MFC actuators on the bimorph swimming system (5).

The composite beam is attached via a clamp to a horizontal arm that pivots about a knife edge (6). A compliant, preloaded spring and counterweight are attached to the opposite end of the horizontal arm (7) to balance the horizontal arm atop the knife edge. This system behaves as a rudimentary balance that will rotate the horizontal arm in response to an unbalanced force, such as when positive or negative thrust is produced by the bimorph swimming system. This behavior is represented in Figure 3.20

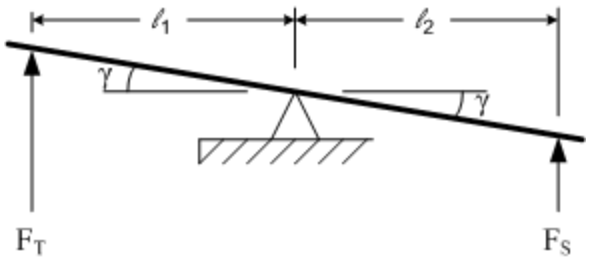

FIGURE 3.20 FORCES APPLIED TO THRUST MEASUREMENT SYSTEM DURING EXPERIMENTS.

The force F_T applied to the horizontal arm is the hydrodynamic thrust force produced by the composite beam as it vibrates in the fluid. The application of the hydrodynamic thrust force causes the horizontal arm to rotate an angle γ about the knife edge. This rotation subsequently compresses the preloaded spring, which produces a reactionary force F_S. A moment balance about the knife edge reveals

$$\sum M = 0 = F_T l_1 - F_s l_2 \tag{3.3.1}$$

The definition of spring force is noted and Equation (3.3.1) is rearranged to produce

$$F_T = \frac{l_2}{l_1} k\Delta y \tag{3.3.2}$$

Therefore, as shown in Equation (3.3.2), the thrust produced is directly related to the vertical displacement of the clamped boundary. Moreover, the horizontal arm is attached to a concrete vibration isolation block to provide a rigid support surface for the balance that is not influenced by ambient vibration. By design, the rotation angle is maintained sufficiently small for classical small angle approximations to apply. The components of the hydrodynamic thrust measurement system are shown in detail in Figure 3.21.

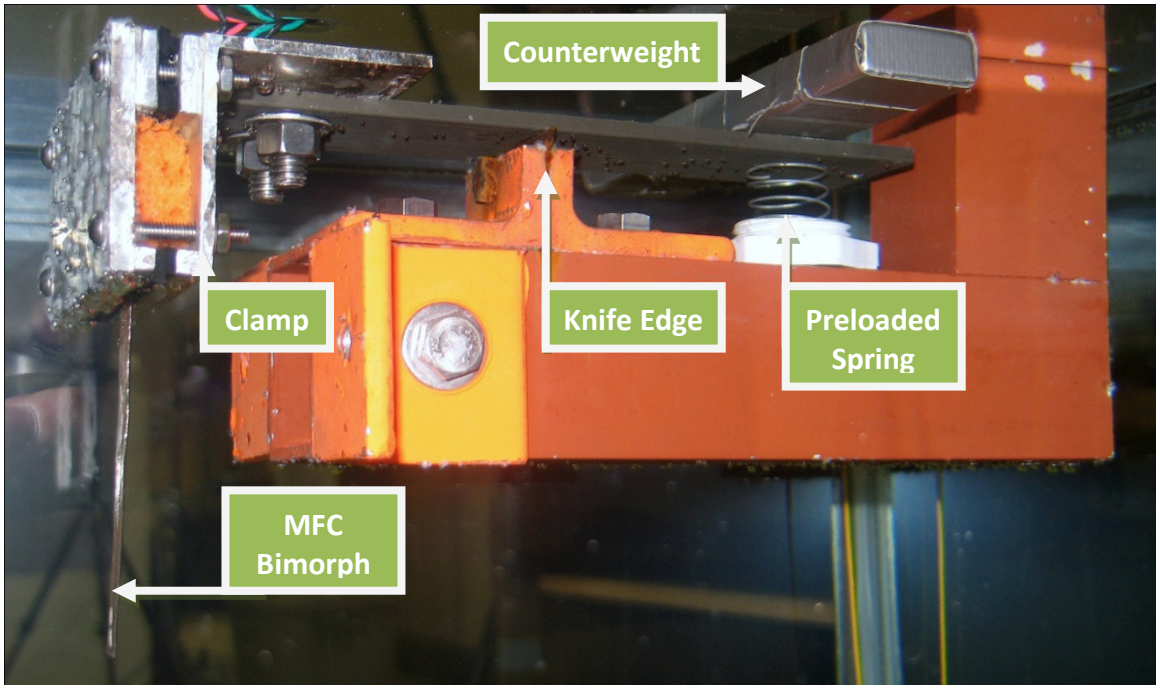

FIGURE 3.21 CLOSE-UP OF THE HYDRODYNAMIC THRUST MEASUREMENT APPARATUS.

An MTI Instruments, Inc. LTC-120-40-SA stand alone laser position sensor (8) placed directly above the bimorph swimming system measures vertical displacement that results from thrust being generated by the bimorph swimming system. The laser position sensor can be seen performing a measurement in Figure 3.22.

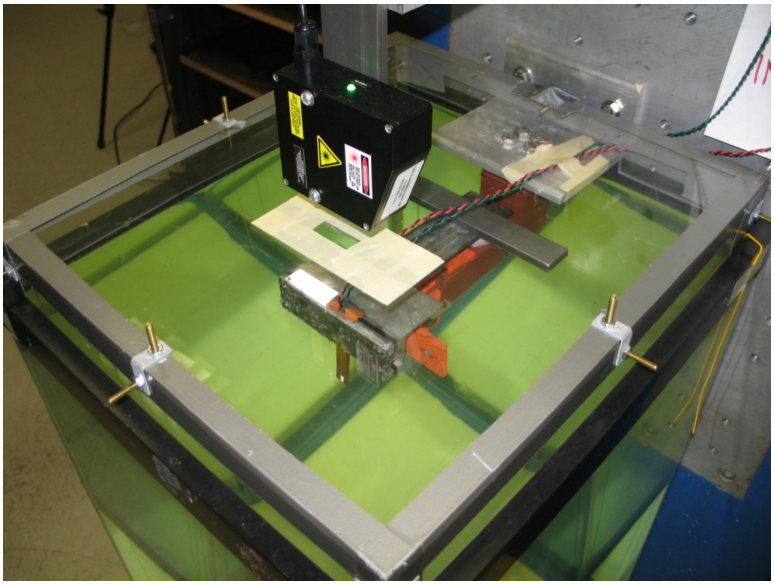

FIGURE 3.22 LASER POSITION SENSOR MOUNT FOR MEASURING CLAMP DISPLACEMENT.

A silver, retro-reflective tape is placed on the clamp's front left edge to reflect the laser beam. Moreover, the top of the aquarium is covered with an acrylic lid to greatly reduce the influence of air currents have on the test apparatus. The signal output from the laser position sensor containing displacement information is then fed to into Input Channel 2 on the voltage input card. The entire experimental apparatus is shown in Figure 3.23.

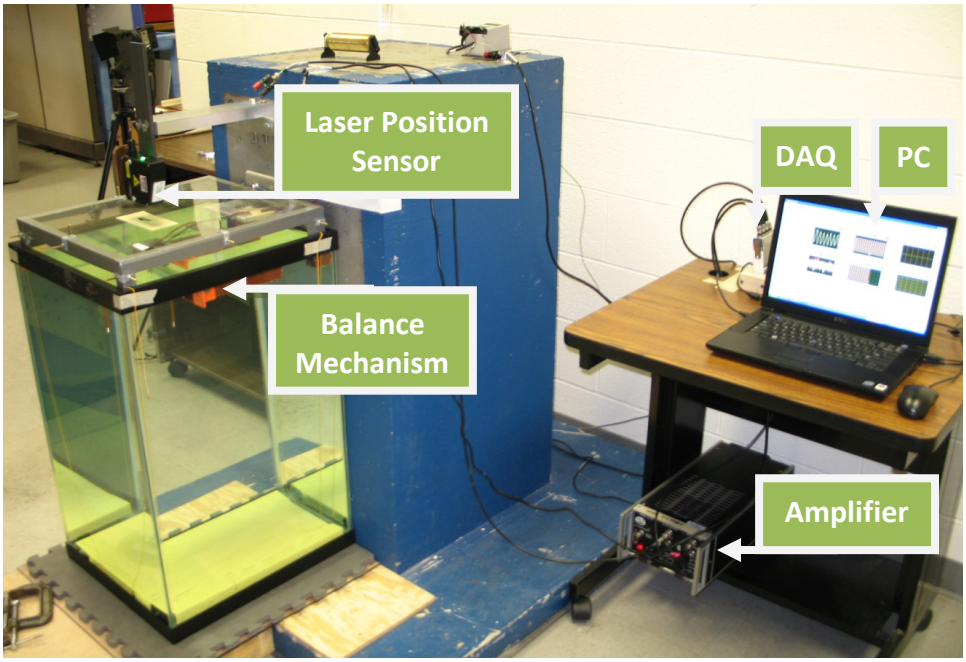

FIGURE 3.23 EXPERIMENTAL SETUP USED TO MEASURE HYDRODYNAMIC THRUST.

Figure 3.23 also displays the manner in which the horizontal arm is affixed to the concrete vibration isolation block.

3.3.2 EXPERIMENTAL TESTING

The LabVIEW program that controls the experimental apparatus is designed to offer the end-user a wide variety of customizability, including the ability to specify excitation voltage, frequency range, and number of experiments to perform for data averaging. The main program provides inputs for a subroutine that divides experimental testing into three phases: pre-calibration, excitation, and post-calibration. Calibration data is acquired before and after each excitation phase to establish the clamped boundary's equilibrium position while the system is at rest. Representative calibration data collected during the pre- and post-calibration phases is shown in Figure 3.24.

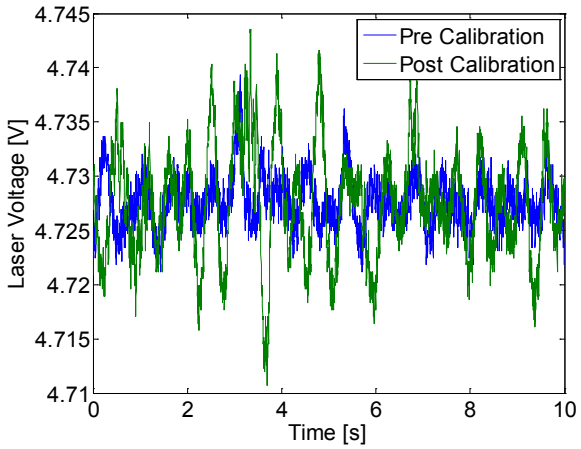

FIGURE 3.24 TYPICAL CALIBRATION PHASE DATA.

Ideally, these two calibration datasets would be constant and identical as the clamped boundary would have returned to the same equilibrium position after the excitation phase. However, ambient vibration and a voltage drift associated with the measurement signal causes the average of the two calibration datasets to differ by approximately 1-3mV. Therefore, the clamped boundary's equilibrium position for an individual experiment is determined to be the position specified by averaging the pre- and post-calibration datasets together.

The excitation phase, which occurs after the pre-calibration phase but before the post-calibration phase, begins with the excitation of the MFC actuators on the composite cantilever beam. Figure 3.25 presents a representative pair of unamplified, excitation signals that are created in LabVIEW and output by the analog voltage output card to drive the MFCs.

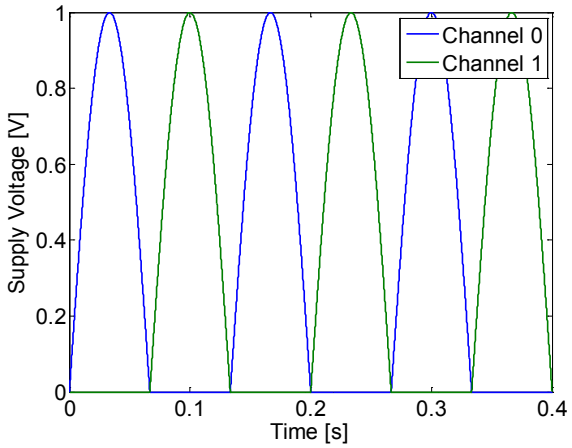

FIGURE 3.25 TYPICAL, UNAMPLIFIED EXCITATION SIGNALS DURING THE EXCITATION PHASE.

The excitation signals shown in Figure 3.25 correspond to the positive half of two sine waves that are 180 degrees out-of-phase with the region where the sine wave would typically become negative is set equal to zero. This out-of-phase actuation pattern effectively doubles the system's peak-to-peak voltage when compared to a unimorph system because the two MFC actuators are excited individually. The maximum peak-to-peak voltage for a MFC actuator is 2kV, which corresponds to the excitation signal spanning from -500V to +1500V. Therefore, the maximum effective peak-to-peak voltage for a bimorph system is 4kV. Increasing the peak-to-peak voltage is advantageous because the deflection and velocity of the composite beam are directly related to the applied voltage.

It should be noted for the actuation pattern shown in Figure 3.25, the maximum effective peak-to-peak voltage is limited to 3kV because the negative portions of the sine waves are set equal to zero. These regions are set equal to zero because the amplifier used in the experiments cannot supply negative voltage. Additionally, due to unexpected actuator failure, each MFC actuator is supplied 1.2kV or less. This corresponds to a maximum effective peak-to-peak voltage of 2.4kV. The actuation signals are generated in LabVIEW with amplitudes ranging from 1-4V in integer increments. Before being routed to the MFCs, these signals pass through an amplifier that has a gain of 300 to produce drive signals with amplitudes ranging from 300-1200V in 300V increments.

Experimental data is collected during the excitation phase once the system has reached its steady-state equilibrium. This eliminates any transience from the experimental data that may skew results from the steady-state behavior that is being examined. The experimental data is collected for ten seconds to ensure that several oscillation cycles are included in the dataset. The first two seconds of typical excitation response data is shown in Figure 3.26.

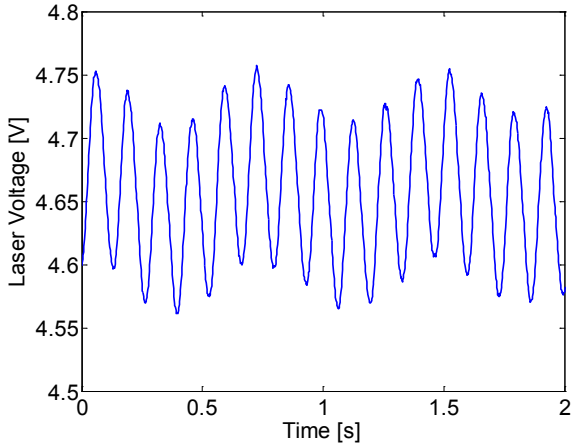

FIGURE 3.26 TYPICAL RESPONSE DATA DURING THE EXCITATION PHASE.

The excitation is ceased once ten seconds of experimental data has been collected. A time delay after the excitation phase allows the system to reach equilibrium before acquiring the post-calibration data. Once an individual frequency has completed all three phases of testing, the main program incrementally moves on to testing the subsequent frequency in the specified measurement range. After each frequency in the specified range have been tested, the main program repeats the experiments multiple times so that several experimental data sets may be averaged together to reduce measurement errors.

Once all the necessary experimental data has been collected, deadweight calibration data is collected to convert the voltage output by the laser sensor into a known load. This process involves placing a series of known weights atop the clamped boundary and onto a point on the horizontal arm near the counterweight that is an equal distance from the system's fulcrum. Weights applied at the clamped boundary cause the balance's equilibrium point to displace downward in response to the negative load while weights applied near the counterweight cause the equilibrium point to displace upward in response to the positive load. The displacements are monitored using the laser displacement sensor and plotted to produce the typical calibration dataset shown in Figure 3.27.

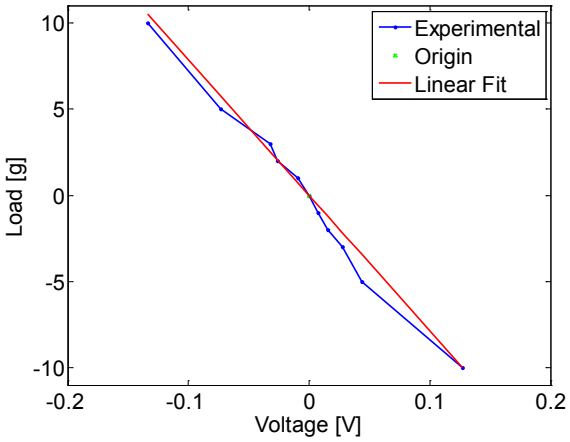

FIGURE 3.27 TYPICAL DEADWEIGHT CALIBRATION DATA.

The linear fit chosen is the best fit available that forces the origin to remain at (0,0). This point is fixed because the voltage presented on the x-axis in Figure 3.27 corresponds to voltage shifts from system's equilibrium position and not to the absolute voltage as output by the laser sensor.

3.3.3 EXPERIMENTAL RESULTS

The experimental data collected via LabVIEW is analyzed in MATLAB. As with the data acquisition phase, the analysis phase is divided into multiple segments. The initial segment loads the appropriate data files from the two calibration phases and the excitation phases. Next, the two calibration datasets are averaged together and the resultant is subtracted from the excitation dataset. This process transfers the excitation data from the absolute coordinate system associated with the laser position sensor to a relative coordinate system centered at the system's equilibrium point. A low pass filter is applied to the calibrated excitation data to filter out unwanted noise, such as 60Hz hum. The filtered, calibrated excitation signal is then truncated to correspond to an integer number of excitation cycles. This signal is then averaged to determine the system's equilibrium point during the excitation phase. If the equilibrium point shifts upwards the device is swimming upward and, conversely, if it shifts downward the device is swimming downward. Lastly, the equilibrium shift is converted to thrust by applying the dead weight calibration and multiplying by gravity.

3.3.3.1 M-8528-P1 Based Systems

The experimentally measured thrust data for an immersed composite cantilever beam with bimorph M-8528-P1 MFC actuators and no substrate vibrating in water is presented in its raw and curve fit forms in Figure 3.28 and Figure 3.29, respectively.

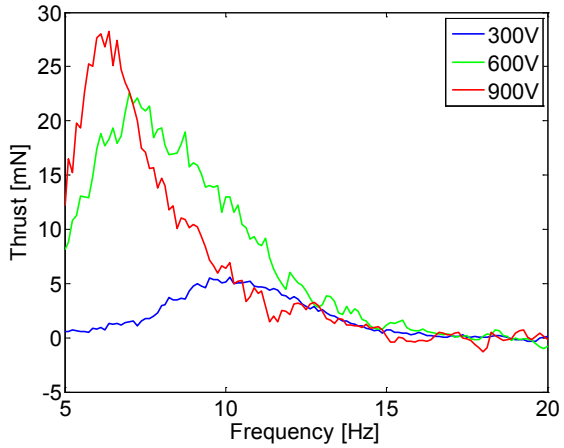

Figure 3.28 Raw thrust data for beam with M-8528-P1 MFCs, no substrate.

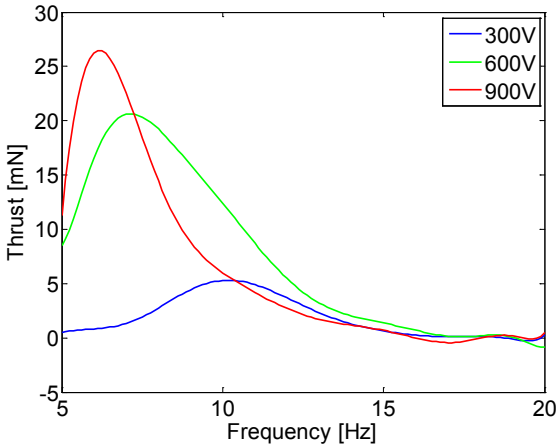

Figure 3.29 Curve fit thrust data for beam with M-8528-P1 MFCs, no substrate

Data is not presented for 1.2kV excitation due to repeated, unexpected actuator failure at this excitation voltage for the M-8528-P1 composite beam with no substrate. It is apparent from these figures that the maximum thrust produced by the device increases as the excitation voltage increases. However, lower excitation voltages may produce larger thrust than higher excitation voltages at certain frequencies. Additionally, the frequency that produces the maximum amount of thrust decreases as the excitation voltage increases.

Similar results are obtained by analyzing the raw and curve fit experimental thrust data for an immersed composite cantilever beam with bimorph M-8528-P1 MFC actuators and a 0.001” thick stainless steel substrate presented in Figure 3.30 and Figure 3.31, respectively.

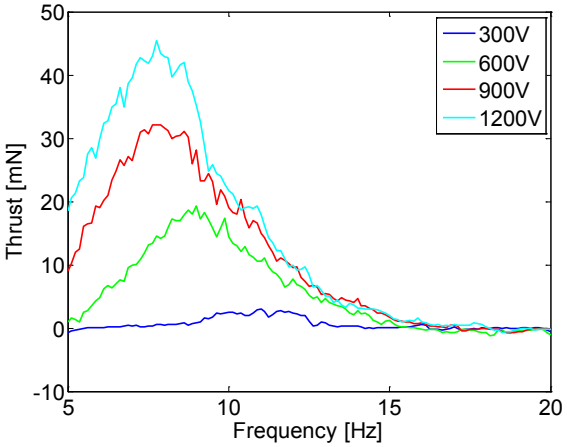

FIGURE 3.30 RAW THRUST DATA FOR BEAM WITH M-8528-P1 MFCS, 0.001" S.S. SUBSTRATE.

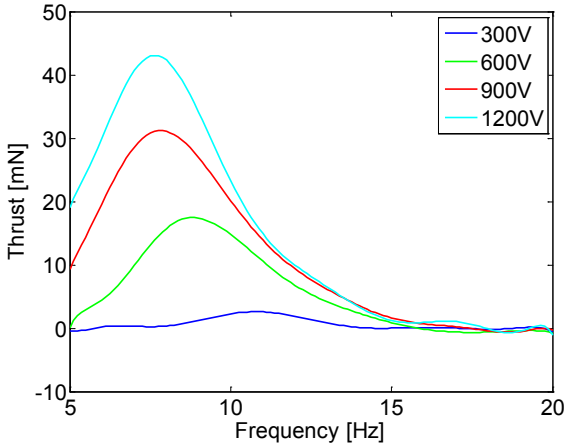

FIGURE 3.31 CURVE FIT THRUST DATA FOR BEAM WITH M-8528-P1 MFCS, 0.001" S.S. SUBSTRATE.

However, unlike the case for the composite beam with M-8528-P1 MFCs and no substrate, the output thrust appears to increase as the excitation voltage increases for all driving frequencies when the composite beam has a substrate. Additionally, the maximum thrust produced by the device is nearly double that produced without a substrate.

3.3.3.2 M-8507-P1 BASED SYSTEMS

The experimentally measured thrust data for an immersed composite cantilever beam with bimorph M-8507-P1 MFC actuators and no substrate vibrating in water is presented in its raw and curve fit forms in Figure 3.32 and Figure 3.33, respectively.

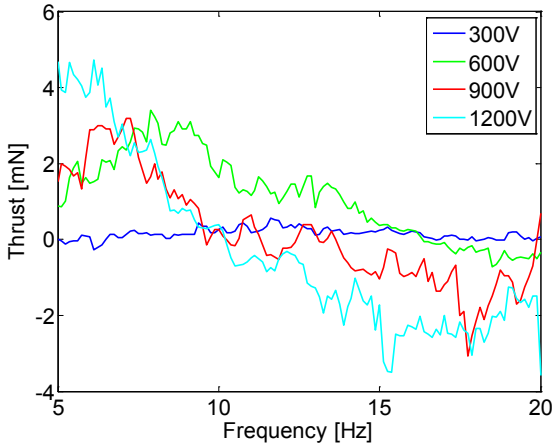

FIGURE 3.32 RAW THRUST DATA FOR BEAM WITH M-8507-P1 MFCS, NO SUBSTRATE.

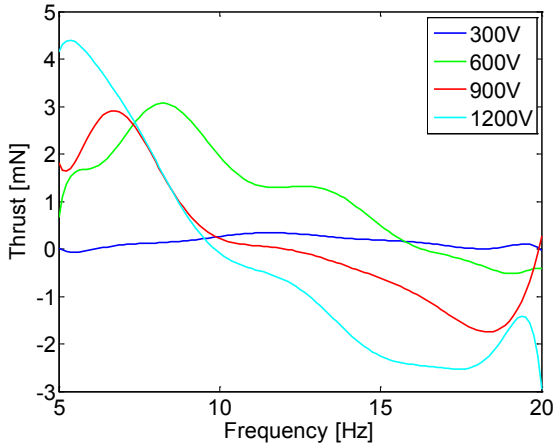

FIGURE 3.33 CURVE FIT THRUST DATA FOR BEAM WITH M-8507-P1 MFCS, NO SUBSTRATE.

The experimental data presented in these figures indicates that a composite beam made with M-8507-P1 MFCs and no substrate is capable of producing both forward and backward thrust. This result was highly unanticipated and may be due to the device twisting during actuation or as a result of pre-strain warping the device's geometry. The previously observed trend that the excitation frequency which maximizes thrust decreases as the excitation voltage increases is also observed herein.

Similar results are obtained by analyzing the raw and curve fit experimental thrust data for an immersed composite cantilever beam with bimorph M-8507-P1 MFC actuators and a 0.001" thick stainless steel substrate presented in Figure 3.34 and Figure 3.35, respectively.

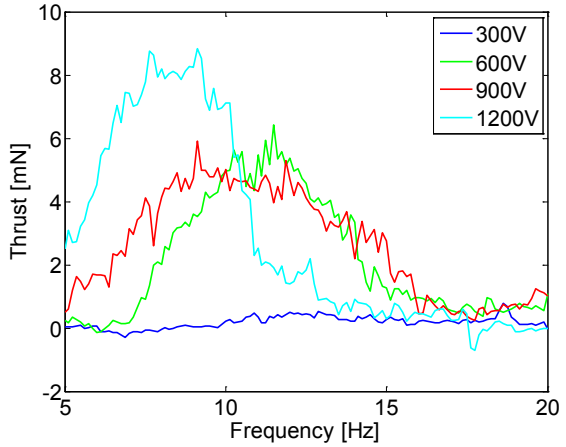

FIGURE 3.34 RAW THRUST DATA FOR BEAM WITH M-8507-P1 MFCS, 0.001" S.S. SUBSTRATE.

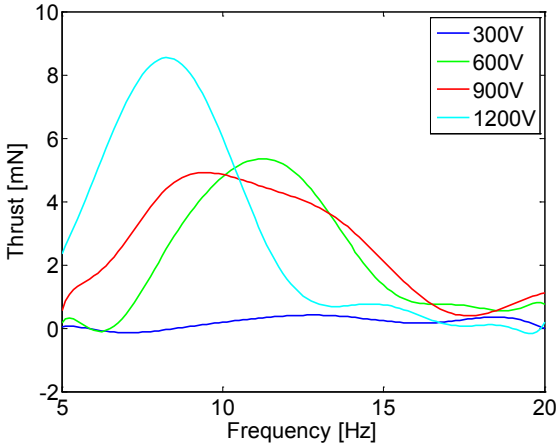

FIGURE 3.35 CURVE FIT THRUST DATA FOR BEAM WITH M-8507-P1 MFCS, 0.001" S.S. SUBSTRATE.

Once again the thrust produced when the system is excited at 600V and 900V is nearly identical. However, unlike the case for the composite beam with M-8507-P1 MFCs and no substrate, the output thrust does not become negative. Additionally, just as with the composite beams made using M-8528-P1 MFCs, the maximum thrust produced by the device is nearly double that produced without a substrate.

3.3.4 COMPARISON TO ANALYTICAL MODEL

The experimentally observed thrust values presented in Section 3.3.3 are compared against thrust values obtained from the analytical model presented in Section 2.4. The analytical thrust model employs the experimental parameters determined in Section 3.2.3. The modal

drag coefficients, just as with the modal damping ratios and piezoelectric forcing coefficients, are determined by matching the analytical model to the experimental data.

3.3.4.1 M-8528-P1 Based Systems

The thrust produced by a composite cantilever beam with bimorph M-8528-P1 MFC actuators and no substrate is shown experimentally and analytically in Figure 3.36.

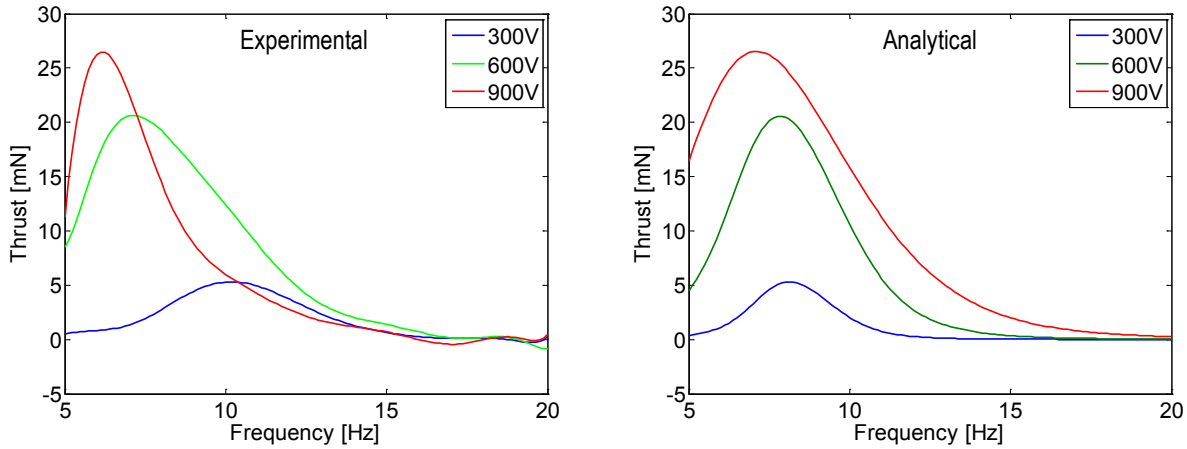

Figure 3.36 Experimental and analytical thrust for M-8528-P1 beam, no substrate.

The modal drag coefficients are chosen such that the thrust amplitude in the analytical model matches that observed experimentally. The modal drag coefficient, maximum thrust, and the corresponding frequency for each excitation voltage are shown in Table 3-10 for both the experimental and analytical cases.

Table 3-10 Thrust results for M-8528-P1 beam, no substrate.

Voltage [V]	Modal Drag Coefficient	Experimental		Model		Frequency Error [%]
		ω_{max} [Hz]	$\bar{F}_{max}$ [mN]	ω_{max} [Hz]	$\bar{F}_{max}$ [mN]	
300	1840	10.13	5.3	8.13	5.3	19.7
600	1780	7.13	20.6	7.88	20.6	10.5
900	3160	6.13	26.5	7.13	26.5	16.3

Overall, the analytical model does not accurately predict the thrust produced by the system. The high degree of error associated with the optimal frequency is likely due to pre-strain in the composite beam that caused the natural frequencies to be much higher than predicted by Euler-Bernoulli beam theory. The width of the peaks as well as their location is also not consistent with the experimental data. However, the analytical model does show the trend that the

optimal excitation frequency decreases as the excitation voltage increases. Moreover, both the experimental data and analytical model indicate that thrust is produced over a wide frequency range.

The thrust produced by a composite cantilever beam with bimorph M-8528-P1 MFC actuators with and a 0.001" thick stainless steel substrate is shown experimentally and analytically in Figure 3.37.

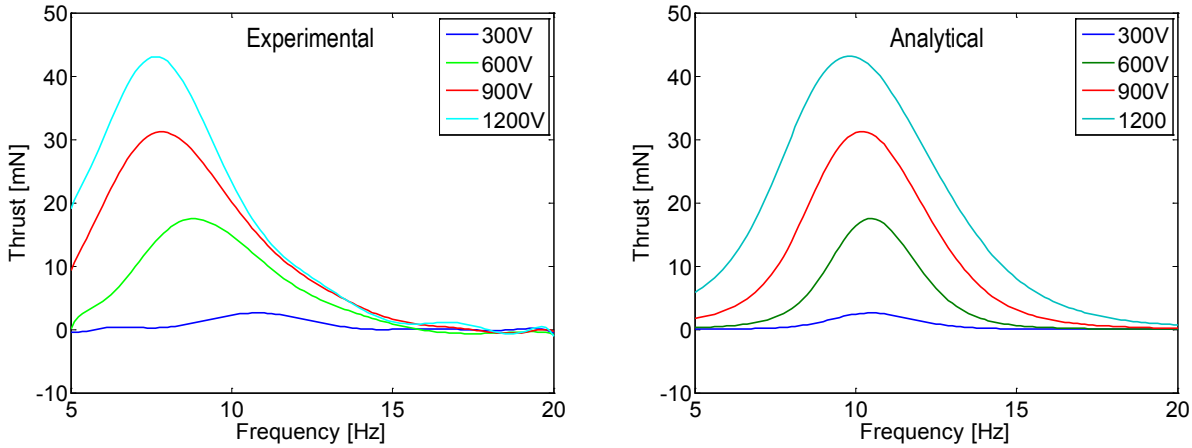

FIGURE 3.37 EXPERIMENTAL AND ANALYTICAL THRUST FOR M-8528-P1 BEAM, 0.001" S.S. SUBSTRATE.

The modal drag coefficient, maximum thrust, and the corresponding frequency for each excitation voltage are shown in Table 3-11 for both the experimental and analytical cases.

TABLE 3-11 THRUST RESULTS FOR M-8528-P1 BEAM, 0.001" S.S. SUBSTRATE.

Voltage [V]	Modal Drag Coefficient	Experimental		Model		Frequency Error [%]
		ω_{max} [Hz]	$\overline{F}_{max}$ [mN]	ω_{max} [Hz]	$\overline{F}_{max}$ [mN]	
300	535	10.75	2.6	10.5	2.6	2.3
600	276	8.88	17.5	10.5	17.5	18.2
900	365	7.88	31.2	10.25	31.2	30.1
1200	486	7.63	43.1	9.75	43.1	27.8

Once again, the model does not accurately predict the thrust produced by the system because the width of the peaks as well as their location does not match the experimental data. The error associated with the frequency that produces the most thrust increases drastically as the excitation voltage increases. Additionally, just as with the case with no substrate, the frequency shift predicted by the model is not as drastic as that observed experimentally. This behavior indicates that the linear and nonlinear damping terms are not accurately represented in the

analytical model. Moreover, additional nonlinearities may be associated with the higher excitation voltages that have not been considered in the analytical model, such as vortex generation.

3.3.4.2 M-8507-P1 Based Systems

The thrust produced by a composite cantilever beam with bimorph M-8507-P1 MFC actuators and no substrate is shown experimentally and analytically in Figure 3.38.

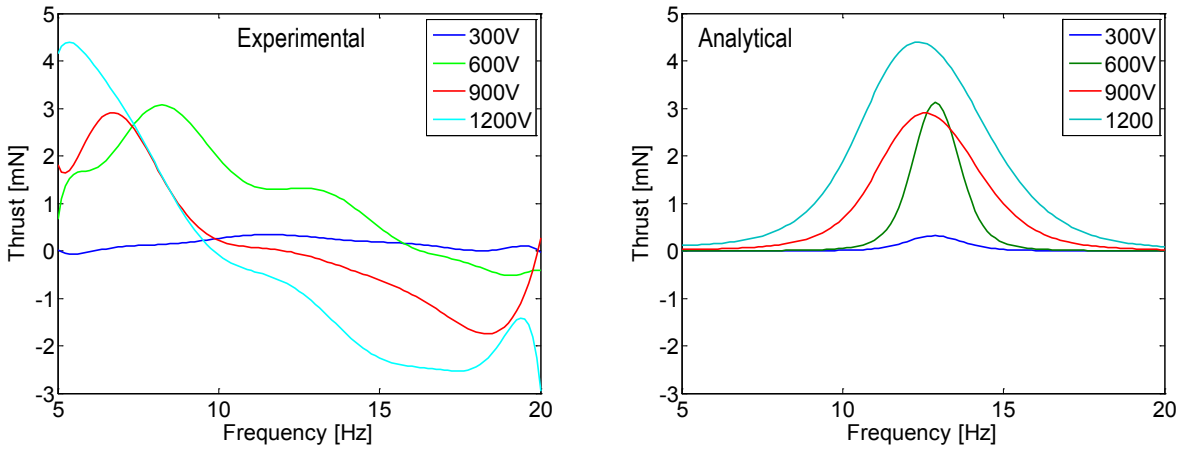

Figure 3.38 Experimental and analytical thrust for M-8507-P1 beam, no substrate.

The modal drag coefficient, maximum thrust, and the corresponding frequency for each excitation voltage are shown in Table 3-12 for both the experimental and analytical cases.

Table 3-12 Thrust results for M-8507-P1 beam, no substrate.

Voltage [V]	Modal Drag Coefficient	Experimental		Model		Frequency Error [%]
		ω_{max} [Hz]	$\bar{F}_{max}$ [mN]	ω_{max} [Hz]	$\bar{F}_{max}$ [mN]	
300	23000	11.63	0.3	12.88	0.3	10.7
600	7100	8.25	3.1	12.88	3.1	56.1
900	25500	6.75	2.9	12.63	2.9	87.1
1200	31000	5.38	4.4	12.38	4.4	130.1

As with the beams made using M-8528-P1 MFCs, the analytical model does not accurately predict the thrust produced by the system. The location and width of the thrust peaks greatly differ from those observed experimentally although their location does shift left as the excitation voltage increases. This shift, however, is not as significant as that observed experimentally and leads to extremely large error as the excitation voltage increases.

Additionally, the analytical model does not predict the regions of negative thrust that were observed experimentally. However, as mentioned previously, these negative regions may be due to the device twisting during actuation or as a result of pre-strain warping the device's geometry.

The thrust produced by a composite cantilever beam with bimorph M-8507-P1 MFC actuators with and a 0.001" thick stainless steel substrate is shown experimentally and analytically in Figure 3.39.

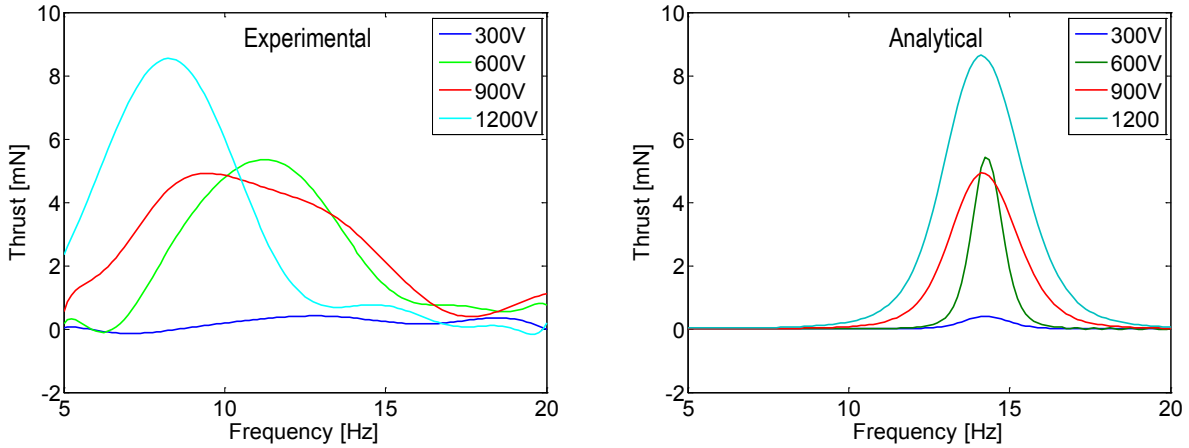

FIGURE 3.39 EXPERIMENTAL AND ANALYTICAL THRUST FOR M-8528-P1 BEAM, 0.001" S.S. SUBSTRATE.

The modal drag coefficient, maximum thrust, and the corresponding frequency for each excitation voltage are shown in Table 3-13 for both the experimental and analytical cases.

TABLE 3-13 THRUST RESULTS FOR M-8507-P1 BEAM, 0.001" S.S. SUBSTRATE.

Voltage [V]	Modal Drag Coefficient	Experimental		Model		Frequency Error [%]
		ω_{max} [Hz]	$\overline{F}_{max}$ [mN]	ω_{max} [Hz]	$\overline{F}_{max}$ [mN]	
300	7500	12.75	0.4	14.25	0.4	11.8
600	1400	11.25	5.4	14.25	5.4	26.7
900	5250	9.5	4.9	14.13	4.9	48.7
1200	5150	8.25	8.6	14.13	8.6	71.3

The analytical results for this configuration, just as with the other configurations, do not match the experimental data particularly well. The thrust peaks continue to remain centered about frequencies much higher than those observed experimentally, although they do shift left as the excitation voltage increases. Additionally, the error associated with these frequencies drastically

increases as the excitation voltage increases because the shift left is not as large as that observed experimentally.

3.3.5 Summary of Thrust Results

The analytical hydrodynamic thrust model does not provide results that correlate sufficiently well with the experimental data to be considered validated. For all but one trial, the thrust peak was centered about a higher frequency than what was observed experimentally. As the excitation voltage increased, the model does predict the frequency that produces the most thrust will shift left from the natural frequency. However, the frequency shifts predicted by the model are not as drastic those observed experimentally. Additionally, the shape and width of the thrust peaks tended to differ significantly from those observed experimentally.

For a simple system, the natural frequencies will only shift left for three possible reasons: an increase in damping, an increase in mass, or a decrease in stiffness. As the stiffness of the composite beam remains constant, the analytical model likely has flaws associated with the added mass term as well as the two damping terms. The added mass term was demonstrated to be valid when examining low amplitude oscillation but it has not been conclusively shown to have the same validity when the system oscillates with larger amplitude. Moreover, a vortex structure is created as the system vibrates that is not considered in the analytical model. This vortex structure can greatly influence the thrust capabilities of the composite beam. Some marine life forms, such as jellyfish, have evolved to produce extremely efficient vortex structures that actually improve their thrust capabilities.

The linear damping term in the hydrodynamic thrust model is assumed to be the net effect of the viscous and strain-rate damping for the composite beam as it operates in air. There may be additional linear damping associated with immersing the device in water that has not been considered in this analysis. Furthermore, the hydrodynamic drag, which is effectively a nonlinear damping, appears to vary more significantly than anticipated as the excitation voltage increase. This is highlighted by the high degree of variation observed in the modal drag

coefficients. These variations may be due to incorrectly computing the coefficients of drag in the normal and tangential directions or due to oversimplifications and omissions in the model.

3.4 CHAPTER SUMMARY

This chapter oversaw the production of the bimorph cantilever beams using MFC actuators as well as two phases of experimental testing aimed at validating the models developed in Chapter 2. The first phase of the experimental testing was designed to validate the added mass assumption used in the analytical models by comparing experimentally measured FRFs to analytically determined FRFs for the devices while they are immersed in water. The analytical model was able to predict the first natural frequency for a composite beam with bimorph MFC actuators to within 7% of that observed experimentally. This relatively small degree of error indicated that the added mass assumption is reasonably accurate. Additionally, this error should decrease with a more complex model for the composite beams bending stiffness and mass distribution. The second phase of the experimental testing produced mixed results as it attempted validate the hydrodynamic thrust model. The model was unable to produce results that agreed well with the experimental data. Nevertheless, the model did predict the frequency that produces the most thrust will decrease as the excitation voltage increases. Although, the frequency shifts predicted were not as large as those observed experimentally. Moreover, several possible sources of error in the analytical model have also been introduced that should be addressed in future studies.

4 PROTOTYPE CARANGIFORM SWIMMER

4.1 OVERVIEW

A prototype carangiform is developed in this chapter using bimorph MFC actuators. The prototype carangiform swimmer differs from the composite beams discussed in the previous sections in that the substrate is patterned after the profile of a carangiform fish. The two main features of such fish are the approximately elliptical body and triangular caudal, or tail, fin. The caudal tail fin is a passive structure that oscillates in response to the body motion and the applied fluidic forces. This passive caudal fin motion, when coupled with the beamlike body motion, produces a swimming motion remarkably similar to that of carangiform fish. This design was originally developed in the Shimojo and Ming Laboratory at the University of Electro-Communications in Japan [50].

4.2 FABRICATION

The prototype carangiform swimmer is made by bonding two M-8528-P1 MFC actuators in bimorph configuration to the fishlike substrate using the same techniques as described in Section 3.1.1. Unlike the composite beams, which used 0.001" thick stainless steel for the substrate, the prototype swimmer uses 0.010" thick stainless steel for the fishlike substrate. A thicker substrate is employed because the caudal fin and portions of the body region are exposed to the environment. If the substrate is too thin these exposed structures will be so compliant that they will not behave as desired. Additionally, the geometry of the fishlike substrate is chosen such that the fish's approximately elliptical body will fully encompass the M-8528-P1 MFC actuator. The dimensions of the caudal fin are chosen to be proportionate with respect to the body of the fish. Moreover as these dimensions are to some degree arbitrarily chosen, the geometry of the device can be optimized to improve results.

The next major hurdle during the fabrication process was designing the prototype swimmer to be buoyant without significantly interfering with the dynamics of the device. These

goals were achieved with a two part floatation system. The first part consists of a clear acrylic cylinder that has been cut along its length is slid atop the body of the fish. The ends of the cylinder are filled with cork to ensure the air chamber will not flood with water during use. The air chamber acts as a ballast tank to help the system become positively buoyant. The second part consists of two foam floats that are attached to the front and rear of the body section to provide additional buoyancy. The finished device is shown in Figure 4.1 and Figure 4.2.

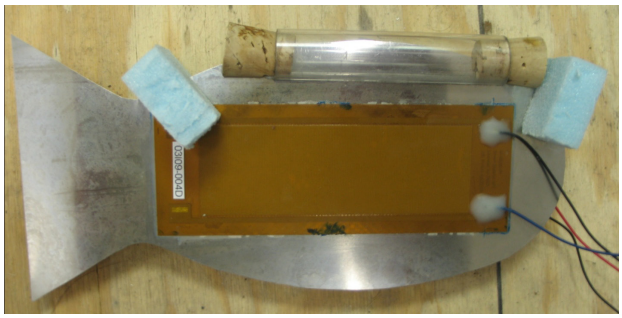

FIGURE 4.1 PROTOTYPE CARANGIFORM SWIMMER.

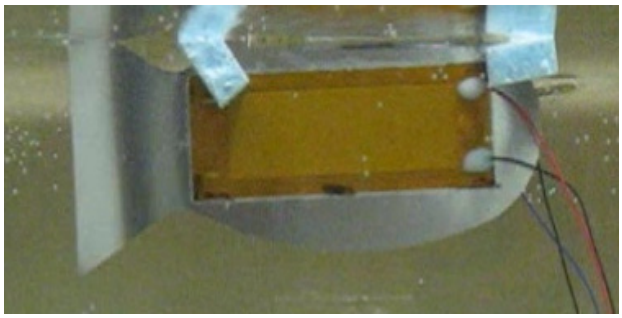

FIGURE 4.2 PROTOTYPE CARANGIFORM SWIMMER FLOATING IN WATER.

When the prototype is placed in water, as shown in Figure 4.2, it is sufficiently buoyant such that waterline comes up to the base of the acrylic cylinder.

4.3 EXPERIMENTAL TESTING & RESULTS

The first step during experimental testing was to determine the excitation frequency that maximized thrust. This was accomplished by placing the prototype in an aquarium and manually stepping the excitation frequency from 0-30Hz in increments of 1Hz while the MFC actuators were supplied the positive half of a sine wave with amplitude 600V. The positive half sine wave excitation signals were of the same form as those used during the excitation phase of the thrust experiments discussed in Section 3.3.2. The prototype was observed to swim the fastest across the aquarium when excited at 20Hz. A series of tests were then conducted with various supply voltages while the device was excited at 20Hz.

TABLE 4-1 EXCITATION VOLTAGE AND SWIM SPEED FOR PROTOTYPE SWIMMER EXCITED AT 20HZ.

Voltage [V]	Velocity [mm/s]
300	≈20
600	≈40
900	≈90

The velocities shown in Table 4-1 are considered approximate because they were obtained from an imprecise analysis on video that was recorded during the experiments. Nevertheless, there is a clear trend that indicates the velocity of the device increases rather significantly with the excitation voltage. Moreover, this trend is obviously nonlinear as the increase in velocity from 600V to 900V is significantly larger than the increase in velocity from 300V to 600V. The experimental data is fitted with a quadratic function and presented in Figure 4.3.

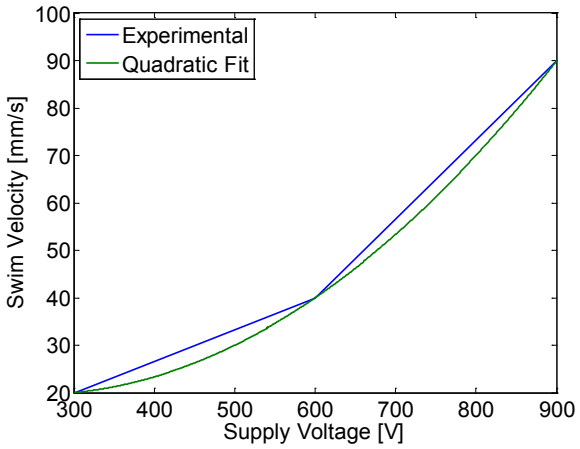

FIGURE 4.3 EXPERIMENTAL AND CURVE FIT PROTOTYPE SWIM SPEED DATA.

The quadratic fit shown in Figure 4.3 well characterizes the nonlinear swim speed behavior that was observed experimentally, which indicates that the swim speed is proportional to the supply voltage squared. This result is unexpected because the analysis in Section 2.4, when continued, indicates that the velocity should be proportional to the applied voltage and not its square. However, it should be noted that as there are so few data points, these points may represent a scatter about a linear trend. Additional data points are required to verify whether this trend is truly quadratic or whether it is linear, as theory would indicate.

4.4 CHAPTER SUMMARY

This chapter oversaw the development and experimental testing of a prototype carangiform swimmer. The net motion of the prototype is more akin to carangiform motion than that of a cantilever beam due to the passive caudal tail. When driven near its experimentally determined first resonant frequency, the prototype's swim speed appeared to scale proportionately with the square of the applied voltage. Moreover, the performance of the carangiform swimmer was in line with that produced in the Shimojo and Ming Laboratory at the University of Electro-Communications in Japan. One swimmer produced in the Shimojo and Ming Laboratory swims at approximately 200mm/s when excited at 25Hz with 900V amplitude. The discrepancy between the experiments herein, which produced 90mm/s swim speeds when excited with 900V amplitude, when compared with those produced at the Shimojo and Ming Laboratory indicate additional geometry optimization is required.

5 SUMMARY & CONCLUSIONS

The objective of this research was to develop a bio-inspired propulsion system for an autonomous underwater vehicle using Macro-Fiber Composite actuators. The design of the propulsion system was inspired by the oscillatory motion of carangiform fish, which rapidly oscillate their caudal tail fin to produce thrust. The initial phase of the research approximated this motion with a cantilever beam that is driven at its fundamental natural frequency. A vibrations model was subsequently developed for an immersed cantilever beam with MFC actuators in bimorph configuration to predict the thrust such a device may produce as a function of both the excitation voltage and frequency. The model coupled Euler-Bernoulli beam theory with linear piezoelectricity and fluid mechanics into a nonlinear partial differential equation. Two fluid mechanics terms were incorporated into the model to address the added mass of the fluid acting on the beam and the nonlinear hydrodynamic drag associated with the beam vibrating in a viscous medium.

A series of experiments were devised to validate the added mass term and the hydrodynamic thrust model. The added mass term was experimentally validated by comparing the analytically derived frequency response function to that obtained experimentally. The hydrodynamic thrust model, however, was not successfully validated. The model was able to predict the experimentally observed trend that the excitation frequency that produces the most thrust decreases as the excitation voltage increases. Unfortunately, it did not accurately predict the excitation frequency that produced the maximum thrust nor did it accurately predict the amount of thrust produced by surrounding frequencies. This was likely due to errors associated with the added mass term while the system vibrates at large amplitude as well as with the linear damping term and the non-linear drag term. Moreover, the experimental apparatus produced a noticeable vortex structure during excitation that was not accounted for in the analytical model. This vortex structure may have significantly influenced the thrust produced by the apparatus as it known to with many marine life forms. Future work should examine these terms individually in an attempt to improve the analytical model.

The final phase of the research oversaw the development and experimental testing of a prototype carangiform swimmer. The prototype, as with the composite beams, employed MFC actuators in bimorph configuration. However, the substrate for the prototype, which was modeled after the profile of carangiform fish, included a passive caudal fin that extended beyond the MFC actuators. The inclusion of the passive caudal fin caused the motion produced by the prototype swimmer to be very similar to that of true carangiform motion. Experimental testing demonstrated the feasibility of the Macro-Fiber Composite actuated carangiform inspired propulsion system. Moreover, the swim speed of the device appeared to scale as a function of the applied voltage and may be improved by optimizing the substrate's geometry.

5.1 CONTRIBUTIONS

Portions of this work were presented at the following technical conference:

1. Hills, Z., M.H. Kim, and D.J. Inman. *Bioinspired Jellyfish Locomotion Using Macro Fiber Composites for Autonomous Underwater Vehicles*. in Proceedings of the ASME 2009 Conference on Smart Materials, Adaptive Structures and Intelligent Systems. 2009. Oxnard, California.

6 BIBLIOGRAPHY

1. Taylor, G., *The Action of Waving Cylindrical Tails in Propelling Microscopic Organisms.* Proceedings of the Royal Society of London. Series A, Mathematical and Physical Sciences, 1952. **211**(1105): p. 225-239.
2. Lighthill, M.J., *Note on the Swimming of Slender Fish.* Journal of Fluid Mechanics, 1960. **9**: p. 305-317.
3. Lighthill, M.J., *Large-Amplitude Elongated-Body Theory of Fish Locomotion.* Proceedings of the Royal Society of London. Series B, Biological Sciences, 1971. **179**(1055): p. 125-138.
4. Sfakiotakis, M., D.M. Lane, and J.B.C. Davies, *Review of fish swimming modes for aquatic locomotion.* Ieee Journal of Oceanic Engineering, 1999. **24**(2): p. 237-252.
5. Mollendorf, J.C., et al., *A fluid/solid model for predicting slender body deflection in a moving fluid.* Journal of Applied Mechanics-Transactions of the Asme, 2003. **70**(3): p. 346-350.
6. Yu, J.Z., S. Wang, and M. Tan, *A simplified propulsive model of bio-mimetic robot fish and its realization.* Robotica, 2005. **23**: p. 101-107.
7. Guo, S., et al., *Development of underwater microrobot using ICPF actuator.* 1998 Ieee International Conference on Robotics and Automation, Vols 1-4, 1998: p. 1829-1834.
8. Guo, S., T. Fukuda, and K. Asaka, *Fish-like underwater microrobot with 3 DOF.* 2002 Ieee International Conference on Robotics and Automation, Vols I-Iv, Proceedings, 2002: p. 738-743.
9. Guo, S., T. Fukuda, and K. Asaka, *A new type of fish-like underwater microrobot.* Mechatronics, IEEE/ASME Transactions on, 2003. **8**(1): p. 136-141.
10. Ye, X.F., et al., *A new type of underwater microrobot driven by single ICPF actuator.* WCICA 2006: Sixth World Congress on Intelligent Control and Automation, Vols 1-12, Conference Proceedings, 2006: p. 8953-8957.
11. Ye, X.F., et al., *ICPF Actuator-based Novel Type of 3D Swimming Microrobot.* 2008 International Conference on Mechatronics and Automation: (Icma), Vols 1 and 2, 2008: p. 556-561.
12. Honda, T., K.I. Arai, and K. Ishiyama, *Micro swimming mechanisms propelled by external magnetic fields.* Ieee Transactions on Magnetics, 1996. **32**(5): p. 5085-5087.
13. Sudo, S., S. Segawa, and T. Honda, *Magnetic swimming mechanism in a viscous liquid.* Journal of Intelligent Material Systems and Structures, 2006. **17**(8-9): p. 729-736.
14. Pan, Q. and S. Guo, *Development of the novel types of biomimetic microrobots driven by external magnetic field.* 2007 IEEE International Conference on Robotics and Biomimetics, Vols 1-5, 2007: p. 256-261.
15. Guo, S., Q. Pan, and M.B. Khamesee, *Development of a novel type of microrobot for biomedical application.* Microsystem Technologies-Micro-and Nanosystems-Information Storage and Processing Systems, 2008. **14**(3): p. 307-314.
16. Zhang, Y.S. and G.J. Liu, *Wireless Swimming Microrobot: Design, Analysis, and Experiments.* Journal of Dynamic Systems Measurement and Control-Transactions of the Asme, 2009. **131**(1).

17. Rediniotis, O.K., et al., *Theoretical and experimental investigations of an active hydrofoil with SMA actuators.* Mathematics and Control in Smart Structures - Smart Structures and Materials 1997, 1997. **3039**: p. 277-289.
18. Rediniotis, O.K., et al., *Development of a spined underwater biomimetic vehicle with SMA actuators.* Smart Structures and Materials 1999: Smart Structures and Integrated Systems, Pts 1 and 2, 1999. **3668**: p. 642-653.
19. Garner, L.J., et al., *Development of a shape memory alloy actuated biomimetic vehicle.* Smart Materials & Structures, 2000. **9**(5): p. 673-683.
20. Webb, G., et al., *Adaptive control of shape memory alloy actuators for underwater biomimetic applications.* AIAA Journal, 2000. **38**(2): p. 325-334.
21. Rediniotis, O.K., et al., *Development of a shape-memory-alloy actuated biomimetic hydrofoil.* Journal of Intelligent Material Systems and Structures, 2002. **13**(1): p. 35-49.
22. Zhang, Y.H., et al., *Development of an underwater oscillatory propulsion system using shape memory alloy.* 2005 IEEE International Conference on Mechatronics and Automations, Vols 1-4, Conference Proceedings, 2005: p. 1878-1883.
23. Zhang, Y.H., et al., *A numerical analysis of an undulatory mechanical fin driven by shape memory alloy.* 2006 IEEE International Conference on Robotics and Biomimetics, Vols 1-3, 2006: p. 73-78.
24. Zhang, S.W., et al., *Computational study on posture control of shape memory alloy biomimetic pectoral fin.* 2007 IEEE International Conference on Mechatronics and Automation, Vols I-V, Conference Proceedings, 2007: p. 497-502.
25. Zhang, Y.H., et al., *Morphologic optimal design of bionic undulating fin based on computational fluid dynamics.* 2007 IEEE International Conference on Mechatronics and Automation, Vols I-V, Conference Proceedings, 2007: p. 491-496.
26. Zhang, Y.H., et al., *Numerical and experimental research on modular oscillating fin.* Journal of Bionic Engineering, 2008. **5**(1): p. 13-23.
27. Ono, N., et al., *Design of fish fin actuators using shape memory alloy composites.* Smart Structures and Materials 2004: Industrial and Commercial Applications of Smart Structures Technologies, 2004. **5388**: p. 305-312.
28. Cho, K.J., et al., *Design, fabrication and analysis of a body-caudal fin propulsion system for a microrobotic fish.* 2008 IEEE International Conference on Robotics and Automation, Vols 1-9, 2008: p. 706-711.
29. Wang, Z., et al., *A micro-robot fish with embedded SMA wire actuated flexible biomimetic fin.* Sensors and Actuators A: Physical, 2008. **144**(2): p. 354-360.
30. Fukuda, T., et al., *Mechanisms and Swimming Experiment of Micro-Mobile Robot in Water.* 1994 Ieee International Conference on Robotics and Automation: Proceedings, Vols 1-4, 1994: p. 814-819.
31. Fukuda, T., et al., *Steering mechanism and swimming experiment of micro mobile robot in water.* Micro Electro Mechanical Systems - IEEE Proceedings, 1995, 1995: p. 300-305.
32. Fukuda, T., et al., *Steering mechanism of underwater micro mobile robot.* Proceedings of 1995 IEEE International Conference on Robotics and Automation, Vols 1-3, 1995: p. 363-368.

33. Borgen, M.G., G.N. Washington, and G.L. Kinzel, *Design and evolution of a piezoelectrically actuated miniature swimming vehicle.* Ieee-Asme Transactions on Mechatronics, 2003. **8**(1): p. 66-76.
34. Heo, S., et al., *Effect of an Artificial Caudal Fin on the Performance of a Biomimetic Fish Robot Propelled by Piezoelectric Actuators.* Journal of Bionic Engineering, 2007. **4**(3): p. 151-158.
35. Wiguna, T., et al., *Experimental parametric study of a biomimetic fish robot actuated by piezoelectric actuators - art. no. 65250R.* Active and Passive Smart Structures and Integrated Systems 2007, 2007. **6525**: p. R5250.
36. Wiguna, T., et al., *Design and Experimental Parameteric Study of a Fish Robot Actuated by Piezoelectric Actuators.* Journal of Intelligent Material Systems and Structures, 2009. **20**(6): p. 751-758.
37. Kosa, G., M. Shoham, and M. Zaaroor, *Propulsion method for swimming microrobots.* IEEE Transactions on Robotics, 2007. **23**(1): p. 137-150.
38. Wilkie, W.K., et al., *Low-cost piezocomposite actuator for structural control applications.* Smart Structures and Material 2000: Industrial and Commercial Applications of Smart Structures Technologies, 2000. **3991**: p. 323-334.
39. High, J.W. and W.K. Wilkie, *Method of Fabricating NASA-Standard Macro-Fiber Composite Piezoelectric Actuators*. 2003.
40. Bilgen, O., K.B. Kochersberger, and D.J. Inman, *Macro-fiber composite actuators for a swept wing unmanned aircraft.* Aeronautical Journal, 2009. **113**(1144): p. 385-395.
41. Bilgen, O., et al., *Novel, Bidirectional, Variable-Camber Airfoil via Macro-Fiber Composite Actuators.* Journal of Aircraft, 2010. **47**(1): p. 303-314.
42. Bilgen, O., A. Erturk, and D.J. Inman, *Analytical and Experimental Characterization of Macro-Fiber Composite Actuated Thin Clamped-Free Unimorph Benders.* Journal of Vibration and Acoustics-Transactions of the Asme, 2010. **Accepted 2010**.
43. Erturk, A., et al., *Piezoelectric Energy Harvesting from Macro-Fiber Composites with an Application to Morphing-Wing Aircrafts*, in *19th International Conference on Adaptive Structures and Technologies*. 2008: Ascona, Switzerland.
44. Wang, D., et al., *Application of macro fibre composite in driving a tail of a biomimetic fish - art. no. 69281H.* Active and Passive Smart Structures and Integrated Systems 2008, 2008. **6928**: p. H9281.
45. Nagata, Y., et al., *Development of Underwater Robot using Macro Fiber Composite.* 2008 Ieee/Asme International Conference on Advanced Intelligent Mechatronics, Vols 1-3, 2008: p. 955-960.
46. Ming, A.G., et al., *Development of an Active Flapping Wing using Piezoelectric Fiber Composites.* 2008 Ieee International Conference on Robotics and Biomimetics, Vols 1-4, 2009: p. 2144-2149.
47. Inman, D.J., *Vibration with Control*. 2 ed. 2007, West Sussex, England: John Wiley & Sons, Ltd.
48. Leo, D.J., *Engineering Analysis of Smart Material Systems*. 2007, Hoboken, New Jersey: John Wiley & Sons, Inc.
49. Blevins, R.D., *Formulas for Natural Frequency and Mode Shape*. 1979, New York, New York: Van Nostrand Reinhold Company, Inc.

50. Shimojo and Ming Laboratory. *MFC Robotic Fish*. [cited 2010 February 1]; Available from: http://www.rm.mce.uec.ac.jp/research/smart/movie/roboticfish.wmv.

APPENDIX A MATLAB CODE

A.1 MAIN.M

```
clear; clc; close all;
%% Choose Test Platform
MFC_Type = 3;        % 1 = M-8528-P1, 3 = M-8507-P1
Substrate = 1;       % 1 = Substrate, 0 = None
FRF_Water = 0;
FRF_Air = 0;

Beam = MFC_Type + Substrate;

if Beam == 1
    BeamDisc = 'BWNS';  MFC = 'M-8528-P1';
    Zeta = .0170;  ZetaF = 0.0065;  Chi = .021;  ScF = .405;  Cd = .025;
elseif Beam == 2
    BeamDisc = 'BWSSS'; MFC = 'M-8528-P1';
    Zeta = .0240;  ZetaF = 0.0195;  Chi = .020;  ScF = .545;  Cd = .095;
elseif Beam == 3;
    BeamDisc = 'BTNS';  MFC = 'M-8507-P1';
    Zeta = .0180;  ZetaF = 0.0075;  Chi = .005;  ScF = .537;  Cd = .0103;
elseif Beam == 4
    BeamDisc = 'BTSSS'; MFC = 'M-8507-P1';
    Zeta = .0089;  ZetaF = 0.0130;  Chi = .005;  ScF = .842;  Cd = .0220;
end

%% Fluid Properties (Wikipedia)
Rho_Air = 1.18;
Rho_Water = 997;
Viscosity = 1.787E-6;

%% Beam Dimensions
BeamDims = 1E-3*[91.5, 40.4, 0.69;
                 89.6, 40.4, 0.79;
                 83.2, 16.2, 0.63;
                 84.3, 16.2, 0.69];

L = BeamDims(Beam,1);
W = BeamDims(Beam,2);
T = BeamDims(Beam,3);

MeasSpot = 1E-3*[6.2;7.05;3.2;4.1];
Xmeas = L - MeasSpot(Beam);
Cam = CoeffAM(L,W);

%% Load Experimental Data
AirData = ['..\Bimorph\Data\',BeamDisc,'\FRF\FRF_Air_',BeamDisc,'.vna'];
WaterData= ['..\Bimorph\Data\',BeamDisc,'\FRF\FRF_Water_',BeamDisc,'.vna'];

[X_Air Y_Air] = FRF_Eval(AirData,25);
```

```
[X_Water Y_Water] = FRF_Eval(WaterData,5);

%% Experimental Frequencies
BeamFreqsAir = [40.63, 232.5;
                38.75, 282.5;
                39.38, 258.1;
                40.63, 264.4];

BeamFreqsWater = [9.875, 64.63;
                  10.63, 87.38;
                  13.88, 94.63;
                  15.38, 102.6];

wr_Exp_Air = zeros(2,1);
wr_Exp_Air(1) = BeamFreqsAir(Beam,1);
wr_Exp_Air(2) = BeamFreqsAir(Beam,2);

wr_Exp_Water = zeros(2,1);
wr_Exp_Water(1) = BeamFreqsWater(Beam,1);
wr_Exp_Water(2) = BeamFreqsWater(Beam,2);

%% Stainless Steel Substrate Material Properties (eFunda)
Rho_Sub = 8000;
E_Sub = 193E9;
if Substrate == 1
    T_Sub = 2.54E-5;
elseif Substrate == 0
    T_Sub = 0;
end
A_Sub = W*T_Sub;
V_Sub = L*A_Sub;
Mx_Sub = Rho_Sub*A_Sub;

%% MFC Properties
T_MFC = 0.3E-3;
if MFC_Type == 1
    W_MFC = 40.4E-3;
    L_MFC = 112E-3;
    M_MFC = 4.1574E-3;
elseif MFC_Type == 3
    W_MFC = 16.2E-3;
    L_MFC = 105E-3;
    M_MFC = 1.2026E-3;
end

Mx_MFC = M_MFC/L_MFC;
E_MFC = 15.857E9;
A_MFC = W*T_MFC;
V_MFC = L*A_MFC;

%% Epoxy Material Properties
Rho_Epoxy = 1094;
E_Epoxy = 3E9;
T_Epoxy = T-2*T_MFC-T_Sub;
A_Epoxy = W*T_Epoxy;
```

```
V_Epoxy = L*A_Epoxy;
Mx_Epoxy = Rho_Epoxy*A_Epoxy;

%% Composite Structure
Sub_Bot = 0;            Sub_Top = T_Sub/2;
Epoxy_Bot = Sub_Top;    Epoxy_Top = Epoxy_Bot + T_Epoxy/2;
MFC_Bot = Epoxy_Top;    MFC_Top = MFC_Bot + T_MFC;

EI = (2/3)*W*(E_Sub*(Sub_Top^3 - Sub_Bot^3) ...
            + E_Epoxy*(Epoxy_Top^3 - Epoxy_Bot^3) ...
            + E_MFC*(MFC_Top^3 - MFC_Bot^3));

Mu = Mx_Sub + Mx_Epoxy + 2*Mx_MFC;
M = Mu + Cam*pi*Rho_Water*W^2/4;

%% Eigenvalues of 1+cos(C)*cosh(C)=0
C = zeros(2,1);
C(1) = 1.875104068711961;
C(2) = 4.694091132974174;
C(3) = 7.854757438237613;
C(4) = 10.995540734875467;
C(5) = 14.137168391046471;

%% Mode Shapes
PhiX_Air = ModeShape(Xmeas,Mu,L,C(1));
PhiX_Water = ModeShape(Xmeas,M,L,C(1));

%% Natural Frequencies
wr_Air = (C(1:2)/L).^2*sqrt(EI/Mu);
wr_Air_Hz = wr_Air/(2*pi);
wr_Air_Error = abs(wr_Exp_Air - wr_Air_Hz)./wr_Exp_Air*100;

wr_Water = (C(1:2)/L).^2 * sqrt(EI/M);
wr_Water_Hz = wr_Water/(2*pi);
wr_Water_Error = abs(wr_Exp_Water - wr_Water_Hz)./wr_Exp_Water*100;

wr = [wr_Exp_Air,   wr_Air_Hz,   wr_Air_Error, ...
      wr_Exp_Water, wr_Water_Hz, wr_Water_Error];

disp(wr)

%% SDOF First Mode Approximation Air
w_Air = 2*pi*X_Air;
G_Air = zeros(length(w_Air),1);
for i = 1:length(w_Air)
    G_Air(i) = abs((-1i*w_Air(i)*PhiX_Air*Chi/...
        (wr_Air(1)^2-w_Air(i)^2+2i*Zeta*wr_Air(1)*w_Air(i)))/(2*pi));
end
if FRF_Air == 1
    figure; plot(X_Air,1E3*Y_Air,X_Air,1E3*G_Air)
    xlim([2 70])
    xlabel('Frequency [Hz]');
    ylabel('Magnitude [mm/s/V]');
    legend('Experiment','SDOF Model');
    if Substrate == 0
        FigTitleA = ['Bimorph ',MFC,' without Substrate (Air)'];
```

```
    elseif Substrate == 1
        FigTitleA = ['Bimorph ',MFC,' with 0.001" Stainless Steel Substrate
(Air)'];
    end
    title(FigTitleA)
end

%% SDOF First Mode Approximation Water
w_Water = 2*pi*X_Water;
S = L*W;
a = 1/2*Rho_Water*S*Cd;
G_Water = zeros(length(w_Water),1);
for i = 1:length(w_Water)
    G_Water(i) = abs((-1i*w_Water(i)*PhiX_Water*Chi*ScF/...
        (wr_Water(1)^2-w_Water(i)^2+2i*(Zeta+ZetaF)*wr_Water(1)*...
         w_Water(i)))/(2*pi));
end
if FRF_Water == 1
    figure; plot(X_Water,1E3*Y_Water,X_Water,1E3*G_Water)
    xlim([5 20])
    xlabel('Frequency [Hz]');
    ylabel('Magnitude [mm/s/V]');
    legend('Experiment','SDOF Model');
    if Substrate == 0
        FigTitleW = ['Bimorph ',MFC,' without Substrate (Water)'];
    elseif Substrate == 1
        FigTitleW = ['Bimorph ',MFC,' with 0.001" Stainless Steel Substrate
(Water)'];
    end
    title(FigTitleW)
end

%% Numerically Integrate to get Drag Coeffs
NumModes = 1;
NumPts = 1E2;
x = linspace(0,L,NumPts); x = x';
dx = L/(length(x)-1);
X = zeros(length(x),1); dX = X;
D = zeros(NumModes,1);
y = zeros(length(x),1);

for i = 1:NumModes
    for j = 1:length(x)
        Phi = ModeShape(x(j),M,L,C(i));
        dPhi = dModeShape(x(j),M,L,C(i));
        if i == 1
            X(j) = Phi;
            dX(j) = dPhi;
        end
    end
end

if Beam == 1
    D = zeros(3,1);
    D(1)=1840; D(2)=1780; D(3)=3160;
elseif Beam == 2
    D = zeros(4,1);
```

```
    D(1)=535; D(2)=276; D(3)=365; D(4)=486;
elseif Beam == 3
    D = zeros(4,1);
    D(1)=23000; D(2)=7100; D(3)=25500; D(4)=31000;
elseif Beam == 4
    D = zeros(4,1);
    D(1)=7500; D(2)=1400; D(3)=5250; D(4)=5150;
end
%% Numerical Integration
w = 2*pi*(5:.125:20);
w=w';
Period = zeros(length(w),1);
IC = [0;0];
U = 0;
Vx = U;
Cn = 1.2;
Options  = odeset('RelTol',1E-9,'AbsTol',1E-10);
PC = ['b';'g';'r';'m'];
V_FRF = zeros(4,length(W));
W_FRF = zeros(4,length(W));

for k = 1:4
    A = k*300;
    for i = 1:length(w)
        tic;
        disp(w(i)/2/pi)
        Period(i) = 2*pi/w(i);
        dt = Period(i)/NumPts;
        PeriodSpan = round(Period(i)/dt);
        Tspan = 0:dt:40*Period(i);
        Vtime = Tspan';
        V = A*sin(w(i)*Vtime);

        [T Y] =
ode15s('BeamODE',Tspan,IC,Options,Vtime,V,wr_Water(1),Zeta,Rho_Water,S,Cd,D,Ch
i*ScF);

        Wxt = Y((end-PeriodSpan):end,1)*X';     Wxt = Wxt';
        Wdt = Y((end-PeriodSpan):end,2)*X';     Wdt = Wdt';
        Wdx = Y((end-PeriodSpan):end,1)*dX';    Wdx = Wdx';
        Time = T((end-PeriodSpan):end)-T(end-PeriodSpan);

        Vz = Wdt;
        Alpha = atan(Wdx);
        Re = zeros(size(Wdt));

        for j = 1:length(x);
            Re(j,:) = abs(Wdt(j,:))*x(j)/Viscosity;
        end

        Re(1,:) = 1;
        Ct = 1.372./sqrt(Re);

        Vn = -Vx.*sin(Alpha) + Vz.*cos(Alpha);
        Vt =  Vx.*cos(Alpha) + Vz.*sin(Alpha);

        dFx = 1/2*Rho_Water*W*(-Ct.*Vt.*abs(Vt)+Cn*Vn.*abs(Vn).*tan(Alpha));
```

```
        Fx = trapz(x,dFx);

        eval(['Fbar_' num2str(k) '_' num2str(i) ' =
trapz(Time,Fx)/Period(i);']);
        eval(['Fbar(k,i) = -Fbar_' num2str(k) '_' num2str(i) ';']);

        V_FRF(k,i) = max(max(abs(Wdt)));
        W_FRF(k,i) = max(max(abs(Wxt)));

        clear Time Tspan Vtime V T Y Wxt Wdt Wdx Re Ct Vn Vt dFx Fx
        toc;
    end
end
figure; plot(w/(2*pi),1E3*Fbar)
ylabel('Thrust [mN]');
xlabel('Frequency [Hz]');
legend('300V','600V','900V','1200V');
```

A.2 MODESHAPE.M

```
function X = ModeShape(x,M,L,C)
Sigma = (sinh(C)-sin(C))/(cosh(C)+cos(C));
X = sqrt(1/(M*L))*(cosh(C*x/L)-cos(C*x/L)-Sigma*(sinh(C*x/L)-sin(C*x/L)));
```

A.3 DMODESHAPE.M

```
function X = dModeShape(x,M,L,C)
Sigma = (sinh(C)-sin(C))/(cosh(C)+cos(C));
X = sqrt(1/(M*L))*(C/L)*(sinh(C*x/L)+sin(C*x/L)-...
    Sigma*(cosh(C*x/L)-cos(C*x/L)));
```

A.4 COEFFAM.M

```
function Cam = CoeffAM(b,a)

Data = [1.00,0.5790; 1.25,0.6419; 1.59,0.7038; 2.00,0.7568; 2.50,0.8008;...
        3.17,0.8404; 4.00,0.8718; 5.00,0.8965; 6.25,0.9167; 8.00,0.9344;...
        10.0,0.9469; 1000,10];

DataSpline = spline(Data(:,1),Data(:,2));
Cam = ppval(DataSpline,b/a);
```

A.5 BEAMODE.M

```
function out = BeamODE(t,y,nothing,Vt,V,wr,zr,rho,S,Cd,Dr,Chir)

V = interp1(Vt,V,t);
eta = y(1);
deta_dt = y(2);
d2eta_dt2 = - wr^2*eta - 2*zr*wr*deta_dt ...
            - 1/2*rho*S*Cd*Dr*abs(deta_dt)*deta_dt - Chir*V;

out = [deta_dt;d2eta_dt2];
```

A.6 FRF_EVAL.M

```
function [Freq XFcn] = FRF_Eval(Filename,SF)

eval(['load ' char(Filename) ' -mat'])
Freq=SLm.fdxvec;
Freq=Freq(:);
XFcn=SF/1000*abs(SLm.xcmeas(1,2).xfer)/10;
```